

## An elementary model of torus canards

G. Nicholas Benes, Anna M. Barry, Tasso J. Kaper, Mark A. Kramer, and John Burke<sup>a)</sup>

*Department of Mathematics and Statistics, Center for BioDynamics, Boston University, Boston, Massachusetts 02215, USA*

(Received 11 September 2010; accepted 29 April 2011; published online 27 June 2011)

We study the recently observed phenomena of torus canards. These are a higher-dimensional generalization of the classical canard orbits familiar from planar systems and arise in fast-slow systems of ordinary differential equations in which the fast subsystem contains a saddle-node bifurcation of limit cycles. Torus canards are trajectories that pass near the saddle-node and subsequently spend long times near a repelling branch of slowly varying limit cycles. In this article, we carry out a study of torus canards in an elementary third-order system that consists of a rotated planar system of van der Pol type in which the rotational symmetry is broken by including a phase-dependent term in the slow component of the vector field. In the regime of fast rotation, the torus canards behave much like their planar counterparts. In the regime of slow rotation, the phase dependence creates rich torus canard dynamics and dynamics of mixed mode type. The results of this elementary model provide insight into the torus canards observed in a higher-dimensional neuroscience model. © 2011 American Institute of Physics. [doi:10.1063/1.3592798]

**Rhythms, and the transitions between different types of rhythms, are central objects of study in biology, chemistry, and neuroscience. Often these systems exhibit multiple time scales, resulting in so-called fast-slow systems. Rhythms in fast-slow systems typically consist either of alternating fast and slow segments or of fast oscillations whose amplitudes are modulated on longer time scales. In this article, we study the latter, specifically slow amplitude modulation of rapid oscillations in fast-slow systems which possess a family of attracting limit cycles and a family of repelling limit cycles. Normally, the attracting limit cycles are of primary importance, since they are the attractors for these systems. However, the repelling limit cycles also play crucial roles, in that they serve as boundaries between the basins of attraction of different attractors. Also, repelling limit cycles turn out to be crucial to the recently discovered phenomenon of torus canards. Torus canards spend long times near slowly varying families of attracting limit cycles and then near slowly varying families of repelling limit cycles, in alternation. They are the natural analog to the classical canards, which arise in the van der Pol equation and other planar, bistable models. The key ingredient for torus canards to occur is that the families of attracting and repelling limit cycles meet in a fold curve, also referred to as a saddle-node bifurcation of limit cycles. Torus canards have been observed in a mathematical model of action potential generation in Purkinje cells. Stable torus canard solutions exist for open sets of parameter values, correspond to amplitude-modulated spiking of the neural dynamics, and arise exactly in the transition region between rapid spiking and bursting in this model. Torus canards may appear in other bistable systems relevant to science and**

**engineering, such as in nonlinear optics, and may further understanding of mixed-mode oscillations (MMO) and the dynamics in the transition region between different types of oscillations.**

### I. INTRODUCTION

Canards are ubiquitous in systems exhibiting multiple time scales, see Refs. 2, 3, 6, 8, 14, 17–19, 27, 36–38, 43, 44, and 53 for some of the references. They were originally discovered<sup>3,14</sup> in the van der Pol equation and arise generically when systems undergo Hopf bifurcations from spiral fixed points to full-blown periodic orbits of relaxation oscillation type. These canard solutions are periodic orbits that exist in narrow intervals of parameter values near the Hopf bifurcation point, and, most interestingly, these orbits spend long times near repelling slow manifolds.<sup>2,13,18,37</sup> Other planar systems possessing canards include the FitzHugh-Nagumo equation,<sup>29</sup> the Bonhoffer-van der Pol equation,<sup>5</sup> and the Kaldor equation.<sup>25</sup>

Canards also play central roles in systems exhibiting mixed-mode oscillations, see Refs. 7, 8, 12, 19, 26, 27, 44, and 53, as well as articles in the focus issue of Chaos.<sup>7</sup> Primary and secondary canards in these systems are the boundaries demarcating the regimes corresponding to periodic orbits with different numbers of small-amplitude oscillations (SAO) and large-amplitude oscillations (LAO). For example, these equations possess periodic orbits with a certain number of SAO followed by one LAO, as well as periodic orbits with the same number of SAO followed by two LAO, and the boundary between these two parameter regimes is given by a family of canards. Moreover, it is worth noting that these canards must exist in order for the property of continuous

<sup>a)</sup>Author to whom correspondence should be addressed. Electronic mail: [jb@math.bu.edu](mailto:jb@math.bu.edu).

dependence of solutions on parameters to be preserved, just as for the van der Pol equation.<sup>3,14</sup>

In essentially all planar systems in which canards are known to occur, the critical underlying structure is that of a curve of attracting fixed points in the fast subsystem which merges with a curve of repelling fixed points at a fold (a.k.a., saddle-node) bifurcation. Indeed, in the van der Pol and other bistable planar systems, the cubic-like fast null-clines are the curves of fixed points, with the outer branches being attracting and the middle one repelling. Canard solutions spend long times near the middle, repelling branch. In systems with two slow variables and one fast variable, there are surfaces of attracting fixed points that merge with surfaces of repelling fixed points in curves of fold points, such as arise in the systems with MMO. There can also be MMO in systems with one slow and two fast variables, see for example Ref. 27.

In this article, we examine the geometrically more complex situation in which families of attracting and repelling limit cycles (rather than fixed points) merge in a fold of limit cycles. The canards that arise are torus canards. They spend long times near the families of both attracting and repelling limit cycles, and they possess two frequencies, one intrinsic to the limit cycles and the other intrinsic to the alternation of fast jumps and slow segments.

Torus canards were recently identified in a biophysical model of the Purkinje cell,<sup>36</sup> which is a neuron found in the cerebellar cortex (other mathematical models exploring bifurcations in Purkinje cells include Refs. 22–24). This model, briefly reviewed in Sec. II, consists of five first-order ordinary differential equations (ODEs), for the voltage, three gating variable corresponding to fast ionic currents, and one gating variable corresponding to a slow ionic current. Torus canards manifest themselves as quasi-periodic oscillations and appear during the transition between the bursting and rapid spiking states of the Purkinje cell model. As discussed in Ref. 36, the presence of torus canards may suggest some biophysical mechanisms that govern the activity in more realistic models of Purkinje cells. In many neural models, complicated dynamics often appears in the transition interval between bursting and rapid spiking states, so a better understanding of torus canards may contribute to the general study of these transitions, as well.

Our main contribution here is to analyze an example of torus canards in a more rudimentary setting, which allows us to develop new insights into the results of Ref. 36. We begin with an extremely simple third-order system of ODEs which is obtained by rotating a planar system of van der Pol type about the axis corresponding to the slow recovery variable. As expected, we find that these torus canards are simply rotations of the classical canards of the planar problem, so all the known results from the planar case carry over in a straightforward way. In particular, the family of canards exists here in an exponentially narrow interval of the bifurcation parameter.

We now introduce the main model of interest in this article. It is obtained by breaking the rotational symmetry in a rotated planar system of van der Pol type,

$$\dot{r} = r(z - f(r)), \quad (1a)$$

$$\dot{\theta} = \omega, \quad (1b)$$

$$\dot{z} = \varepsilon \left( a - \sqrt{r^2 - 2rb \cos \theta + b^2} \right), \quad (1c)$$

where  $f(r) = 2r^3 - 3r^2 + 1$ , and  $\varepsilon, \omega, a, b$  are parameters with  $0 < \varepsilon \ll 1$ . The symmetry breaking term in system (1) is specifically chosen to shift the null-surface of the slow  $z$  variable by a distance  $b$  in the Cartesian  $x$ -direction. The voltage-like variable in this system is the cartesian  $y$  coordinate, so  $r$  measures the amplitude or envelope of the underlying oscillation. In what follows, we show that the symmetry breaking term is the key feature that gives rise to nontrivial torus canards and MMO. In particular, we will show that the parameter regime in which torus canards exist in system (1) is measurably larger than in the rotationally symmetric case, and the alternations between LAO and SAO are rich, since these transitions now also depend on orbital phase.

We will show that the dynamics of torus canards in the third-order system (1) depends critically on  $\omega$ , the rate of rotation. For fast rotations, the canards exist only in narrow intervals of parameter values, similar to the rotationally symmetric case. In contrast, it is in the regimes of intermediate and slow rotations that we find a wide range of dynamics of torus canards and MMO. We present a combination of analytical and numerical results to explore the behavior of torus canards in these different regimes.

The results we obtain for system (1) also yield new insight into the dynamics of the torus canards observed in the Purkinje cell model of Ref. 36. Specifically, we will show that in system (1) torus canards and MMO become more robust when the rotation rate  $\omega$  decreases, and we find a similar result when we decrease the spike frequency for the fifth-order Purkinje cell model. We refer the reader to Refs. 1, 11, 32, 33, 40, 46, 50, and 52 for general treatments of bursting in mathematical models in neuroscience, as well as to Refs. 47 and 48 for canards in maps, another class of problems for which the analysis here may have further implications.

It is possible to convert system (1) into a two-dimensional forced oscillator by integrating the  $\dot{\theta}$  component. The results presented here for system (1) complement those presented earlier in Refs. 4 and 27, where a different class of forced van der Pol oscillators is studied. In those works, the forcing replaces the parameter  $a$  from the planar system with an effective value of  $a \sin(\omega t)$ , so the amplitude of the forcing is large and the slow null-cline moves back-and-forth between the two outer (attracting) branches of the fast null-cline each period. The analogous forcing term in the system studied here is, for small  $b$ , given by  $a + b \cos(\omega t)$ , so the slow null-cline remains in the neighborhood of a fold of the fast null-cline.

This article is organized as follows. In Sec. II, we review the torus canard phenomena as observed in Ref. 36. In Sec. III, we briefly present results for the simple rotated planar system. In Sec. IV, we present the main third-order model studied in this article and describe the torus canards that it possesses. The analyses of the regimes of fast rotation and slow rotation are given in Secs. V and VI, respectively. In Sec. VII, we show that our conclusions carry over to a large class of systems with general phase-dependent

symmetry breaking terms. Finally, in Secs. VIII and IX, we present some of the implications of our main results for the Purkinje model, and we discuss some other conclusions and open questions.

## II. MOTIVATION: PURKINJE MODEL

In this section, we briefly describe the torus canard phenomenon as observed in an elementary biophysical model of a Purkinje cell.<sup>36</sup> This single-compartment model consists of five ODEs that describe the dynamics of the membrane potential ( $V$ ) and four ionic gating variables ( $m_{\text{CaH}}$ ,  $h_{\text{NaF}}$ ,  $m_{\text{KDR}}$ , and  $m_{\text{KM}}$ )

$$C \dot{V} = -J - g_L(V - V_L) - g_{\text{CaH}} m_{\text{CaH}}^2 (V - V_{\text{CaH}}) - g_{\text{NaF}} m_{\text{NaF}}^3 h_{\text{NaF}} (V - V_{\text{NaF}}) - g_{\text{KDR}} m_{\text{KDR}}^4 (V - V_{\text{KDR}}) - g_{\text{KM}} m_{\text{KM}}^4 (V - V_{\text{KM}}), \quad (2a)$$

$$\dot{m}_{\text{CaH}} = \alpha_{\text{CaH}}(1 - m_{\text{CaH}}) - \beta_{\text{CaH}} m_{\text{CaH}}, \quad (2b)$$

$$\dot{h}_{\text{NaF}} = \alpha_{\text{NaF}}(1 - h_{\text{NaF}}) - \beta_{\text{NaF}} h_{\text{NaF}}, \quad (2c)$$

$$\dot{m}_{\text{KDR}} = \alpha_{\text{KDR}}(1 - m_{\text{KDR}}) - \beta_{\text{KDR}} m_{\text{KDR}}, \quad (2d)$$

$$\dot{m}_{\text{KM}} = \alpha_{\text{KM}}(1 - m_{\text{KM}}) - \beta_{\text{KM}} m_{\text{KM}}. \quad (2e)$$

The parameter  $J$  represents an externally applied current, with decreased values corresponding to excitation and increased values to inhibition. The forward and backward rate functions ( $\alpha_X$  and  $\beta_X$  for  $X = \text{CaH}, \text{NaF}, \text{KDR}, \text{KM}$ ) and fixed parameters in Eq. (2a) are defined in Appendix. The gating variable  $m_{\text{KM}}$  for the muscarinic receptor suppressed potassium current (a.k.a., M-current) evolves on a much slower time scale than the other variables. As such, the dynamics in this five-dimensional model can be understood in part by studying the four-dimensional fast subsystem, which is defined by setting  $\dot{m}_{\text{KM}} = 0$  and treating  $m_{\text{KM}}$  as a bifurcation parameter in the remaining equations.

Figure 1 shows the behavior of the full Purkinje model at three different values of  $J$ , corresponding to examples of rapid spiking, amplitude modulated spiking, and bursting. In each case, the figure includes a time series of the voltage from the full model and the bifurcation diagram for the fast subsystem. The former are computed by numerically integrating system (2) with an arbitrary initial condition and disregarding the transient. The latter are traced out by continuation methods using AUTO (Ref. 15). Each bifurcation diagram includes a branch of attracting fixed points which merges with a branch of repelling fixed points in a

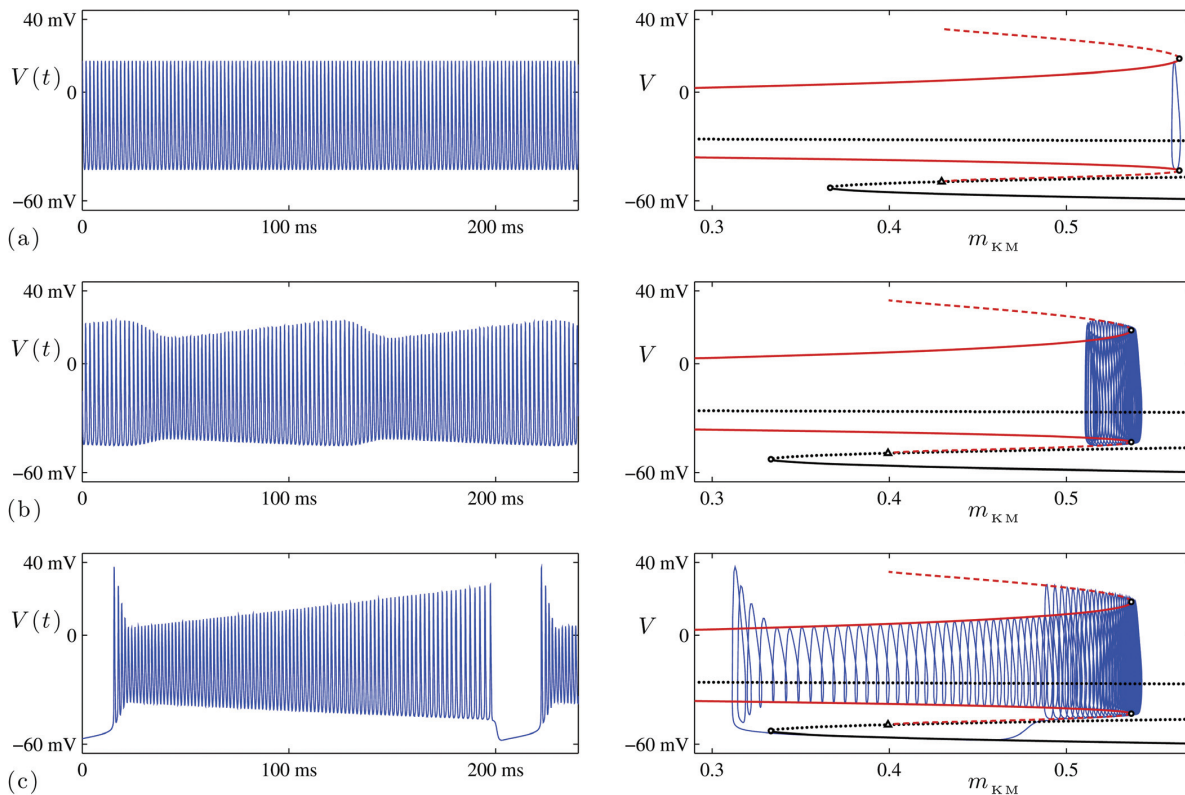


FIG. 1. (Color online) Behavior of the Purkinje cell model (2) at three different values of  $J$ : (a) rapid spiking, at  $J = -34$  nA; (b) amplitude modulated spiking, at  $J = -32.94$  nA; (c) bursting, at  $J \approx -32.93$  nA. In each case, the left panel shows the time-series of the voltage, and the right panel shows the bifurcation diagram of the corresponding fast subsystem with the trajectory from the full system superimposed. In the fast subsystem, the branches of attracting (solid line) and repelling (dotted line) fixed points merge in a fold ( $\triangle$ ). The branches of attracting (solid line) and repelling (dashed line) limit cycles merge in a fold of limit cycles ( $\circ$ ). The branch of repelling limit cycles terminates on the branch of repelling fixed points in a homoclinic bifurcation ( $\Delta$ ). Two curves are plotted for each branch of limit cycles, indicating the maximum and minimum values of  $V$  over the period.

fold of fixed points and a branch of attracting limit cycles which merges with a branch of repelling limit cycles in a fold of limit cycles. Topologically, the branches of limit cycles are cylinders but for simplicity we plot only the maximum and minimum values of  $V$  over the period. In each case, the solution of the full system is also shown superimposed on the bifurcation diagram of the fast subsystem, and it is this composition which provides the most insight into the dynamics in each regime.

For  $J$  sufficiently small (excitatory), trajectories of the full system approach a stable limit cycle which corresponds to rapid spiking of the neuron (Fig. 1(a)). The slow variable  $m_{\text{KM}}$  is nearly constant in this state, and the trajectory of the full system closely resembles an orbit from the branch of stable limit cycles of the fast subsystem. At a larger value of  $J$ , the system undergoes amplitude modulated spiking (Fig. 1(b)). In this case, the trajectory closely follows the branch of attracting limit cycles of the fast subsystem as  $m_{\text{KM}}$  slowly increases to the fold point, then follows the branch of repelling limit cycles as  $m_{\text{KM}}$  slowly decreases beyond the fold. Eventually, the trajectory leaves this repelling branch and quickly transitions back to the attracting branch of limit cycles, restarting the sequence. Further increase in  $J$  introduces an interval of quiescence in the full dynamics (Fig. 1(c)). This occurs when the trajectory leaves the fast subsystem's branch of repelling limit cycles and approaches the branch of attracting fixed points (rather than the branch of attracting limit cycles). The quiescence ends when the trajectory reaches the fold of fixed points and quickly transitions back to the branch of attracting limit cycles. This pattern of quiescence and rapid spiking repeats to generate bursting activity in the full system. Finally, we note that for  $J$  sufficiently large (inhibitory) the Purkinje cell model exhibits unmodulated quiescence corresponding to a stable fixed point of the system (not shown).

The transition from stable rapid spiking to stable amplitude modulated spiking occurs via a supercritical torus bifurcation in the full system, as shown in Ref. 36. The growth of amplitude modulated spiking and the eventual transition to bursting in this model involves torus canards. These arise at precisely those  $J$  values for which certain invariant manifolds intersect. In particular, Fenichel theory yields that outside a neighborhood of the fold of limit cycles, the cylinders of attracting and repelling limit cycles in the fast subsystem persist as attracting and repelling invariant manifolds when  $m_{\text{KM}}$  evolves slowly, say  $\dot{m}_{\text{KM}} = \mathcal{O}(\epsilon)$ . These persistent invariant manifolds are smooth and located a small  $\mathcal{O}(\epsilon)$  distance away from the cylinders of the fast subsystem. The persistent invariant manifolds can be extended into the neighborhood of the fold of limit cycles by flowing orbits on them forward and backward in time. A torus canard is a trajectory that spends long time near the attracting manifold, passes through the fold, then spend long time near the repelling manifold; thus, torus canards occur whenever the attracting and repelling manifolds intersect.

### III. THE ROTATED PLANAR SYSTEM

In this section, we introduce one of the simplest third-order systems that possesses torus canards, namely we con-

sider a planar system of van der Pol type, rotated about the axis corresponding to the slow recovery variable

$$\dot{r} = r(z - f(r)), \quad (3a)$$

$$\dot{\theta} = \omega, \quad (3b)$$

$$\dot{z} = \epsilon(a - r), \quad (3c)$$

where  $f(r) = 2r^3 - 3r^2 + 1$  and  $\epsilon, a, \omega$  are parameters with  $0 < \epsilon \ll 1$ . The parameter  $a$  is the control parameter that is important for canard behavior. Away from  $r = 0$  and for any fixed choice of  $\theta$ , the resulting planar cross section of the full system (3) has null-clines which resemble those of the classical van der Pol oscillator. Furthermore, the  $\theta$ -dynamics decouples from the  $r - z$  system, so in the full system one sees the usual dynamics of a van der Pol oscillator except that the fast variable  $r$  is interpreted as the amplitude or envelope of an underlying oscillation with frequency  $\omega$ . The torus canards in Eq. (3) are therefore a trivial extension of planar canards to a three dimensional system, and the important properties of these torus canards (e.g., range of existence) are identical to those in the planar case, as described below.

The phase space of the  $r - z$  system (in the relevant domain  $r > 0$ ) is sketched in Fig. 2. The  $z$ -null-cline consists of the vertical line  $r = a$ . The  $r$ -null-cline consists of two branches—the vertical line  $r = 0$  and the curve  $z = f(r)$ , which has a local maximum at  $(r, z) = (0, 1)$  and a local minimum at  $(r, z) = (1, 0)$ . In general, the flow circulates clockwise around the fixed point at the intersection of the null-clines, at  $(r, z) = (a, f(a))$ .

Within the fast subsystem  $z$  is a fixed parameter, so the  $r$ -dynamics exhibits a subcritical bifurcation at  $(r, z) = (0, 1)$ , with the nontrivial branch restabilized by the cubic term at large amplitude. Thus, trajectories flow away from the

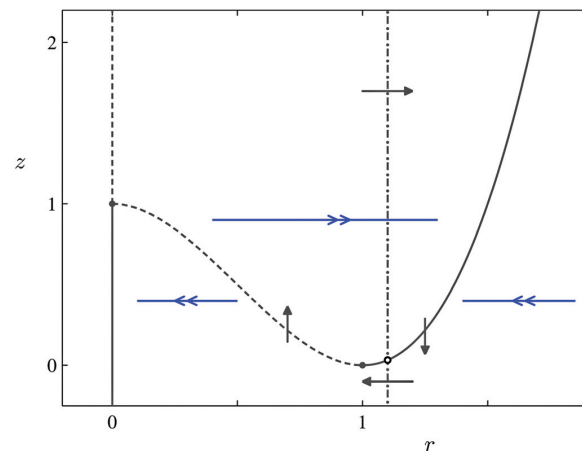


FIG. 2. (Color online) Sketch of the phase space of the  $r - z$  system from Eq. (3), including the null-clines for  $a = 1.1$ . The  $z$ -null-cline is plotted as a dot-dashed line. The  $r$ -null-cline is plotted as a solid (dashed) line where it corresponds to a stable (unstable) fixed point of the fast subsystem. The null-clines intersect at the fixed point  $(r, z) = (a, f(a))$ , marked with the  $\circ$  symbol. The two-dimensional flow across the null-clines is indicated by single arrows, and the one-dimensional flow in the fast subsystem is indicated by double arrows. Only  $r > 0$  is considered.

repelling branches of the  $r$ -null-cline ( $r=0$  in  $z > 1$  and the segment of the  $f(r)$  curve in  $0 < r < 1$ ), rapidly converging to the attracting branches ( $r=0$  in  $z < 1$  and the outer segments of the  $f(r)$  curve).

The fixed point at  $(r, z) = (a, f(a))$  of the  $r - z$  system undergoes a Hopf bifurcation at  $a = 1$ . This may be seen from linear stability analysis. Let  $R$  and  $Z$  be defined by  $(r, z) = (a, f(a)) + (R, Z)$ . The linearization is

$$\begin{bmatrix} \dot{R} \\ \dot{Z} \end{bmatrix} = \mathcal{L} \begin{bmatrix} R \\ Z \end{bmatrix}, \quad \text{where } \mathcal{L} \equiv \begin{bmatrix} -6a^2(a-1) & a \\ -\varepsilon & 0 \end{bmatrix}, \quad (4)$$

so that  $\text{Tr}\mathcal{L} = -6a^2(a-1)$  and  $\text{Det}\mathcal{L} = \varepsilon a$ , and the eigenvalues  $\sigma$  which determine the linear growth rate of perturbations from the fixed point satisfy  $0 = \sigma^2 - \sigma \text{Tr}\mathcal{L} + \text{Det}\mathcal{L}$ . When  $a$  is sufficiently greater than one, both eigenvalues are real ( $(\text{Tr}\mathcal{L})^2 > 4\text{Det}\mathcal{L}$ ) and negative ( $\text{Tr}\mathcal{L} < 0$ ). At  $(\text{Tr}\mathcal{L})^2 = 4\text{Det}\mathcal{L}$ , corresponding to  $a \approx 1 + \varepsilon^{1/2}/3$ , the eigenvalues become complex with  $\text{Re}\sigma < 0$  so the fixed point remains stable. At  $a = 1$ , we have  $\text{Tr}\mathcal{L} = 0$  and  $\sigma = \pm i\varepsilon^{1/2}$  as the eigenvalues cross the  $\text{Im}\sigma$  axis. In  $a < 1$ , the eigenvalues have  $\text{Re}\sigma > 0$ , and the fixed point is unstable. Thus, the fixed point undergoes a Hopf bifurcation at  $a = 1$ . Note that this corresponds in the phase space diagram to the instant when the  $z$ -null-cline crosses the local minimum of the  $r$ -null-cline at  $(r, z) = (1, 0)$ . Using standard techniques of normal-form analysis, one can show that this Hopf bifurcation is always supercritical, so stability is transferred to the branch of small amplitude periodic orbits in  $a < 1$ .

To illustrate the dynamics of this model, various orbits from the branch of limit cycles are shown in Fig. 3, plotted in the  $r - z$  phase space. The amplitude of the limit cycles is small near onset and grows as  $a$  decreases. Eventually, the periodic orbit undergoes a rapid jump in amplitude corresponding to the canard explosion. The bifurcation diagram in Fig. 4(a) summarizes the growth of the periodic orbit. A simple geometric argument explains these results. First, note that Fig. 3 also includes the  $r$ -null-cline, which consists of the branches of attracting and repelling fixed points of the fast subsystem. Fenichel theory yields that outside a neighborhood of the fold at  $(r, z) = (1, 0)$ , these critical manifolds persist as attracting and repelling slow manifolds when  $\varepsilon$  is small but nonzero. These persistent slow manifolds are one-dimensional, so each corresponds to a single trajectory that can easily be extended into the neighborhood of the fold by following the orbit forward or backward in time. Near the Hopf bifurcation, the attracting slow manifold spirals directly in to the small amplitude periodic orbit, so the attracting slow manifold must lie above the repelling slow manifold. At smaller values of  $a$ , where the stable periodic orbit is instead a large amplitude relaxation oscillation, the attracting slow manifold must lie below the repelling slow manifold. Continuity requires that these manifolds pass through each other as  $a$  decreases, and it is this crossing that creates the canard explosion. Canard orbits only occur in the narrow range of  $a$  values for which these manifolds are sufficiently close as to allow a single trajectory to spend considerable time in the neighborhood of both. The *maximal canard* occurs at the unique  $a$  value at which the attracting

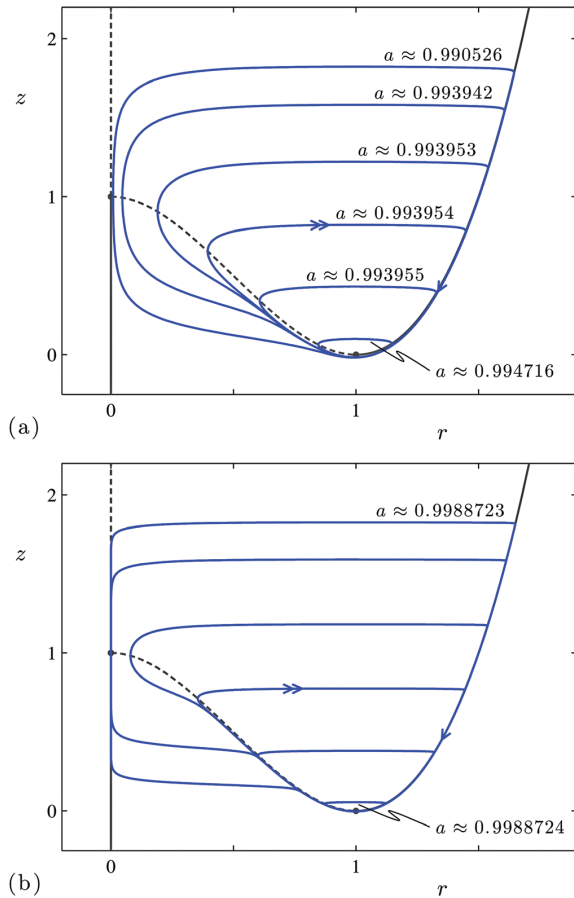


FIG. 3. (Color online) Collection of representative periodic orbits associated with the canard explosion at (a)  $\varepsilon = 0.1$  and (b)  $\varepsilon = 0.02$ . In each panel, the orbits shown represent the limit cycles for a range of  $a$  values rather than solutions at a particular value of  $a$ . The canard explosion shown in (b) is already sufficiently abrupt that all the unlabeled orbits in this panel occur at nearly identical  $a$  values,  $a \approx 0.9988723$ .

and repelling slow manifolds intersect and can be identified in Fig. 4(b) as the limit cycle with the maximum period. Both the location in  $a$  and the abruptness of the explosion are functions of  $\varepsilon$ : for smaller  $\varepsilon$ , the canard explosion occurs closer to  $a = 1$  (i.e., closer to the Hopf point) and in a smaller range of values of  $a$ . Under an appropriate change of variables, the  $r - z$  system from Eq. (3) can be put into the canonical form given by Ref. 37, and the results from that paper predict the maximal canard occurs at  $a \approx 1 - \varepsilon/18$ . For completeness, we note that some of the solutions also have long segments near the repelling branch of the  $z$ -axis, see, for example, the two outermost orbits in Fig. 3(b). Hence, they are also canards because they are near a repelling slow manifold for a long time, although we do not focus on this aspect of the solutions in this work.

The behavior of torus canards in the full three-dimensional system (3) is now clear. In  $a > 1$ , the system contains a stable limit cycle with frequency  $\omega$  and radius  $r = a$ . At  $a = 1$ , the limit cycle becomes unstable in a supercritical torus bifurcation. The tori in  $a < 1$  resemble donut-shaped

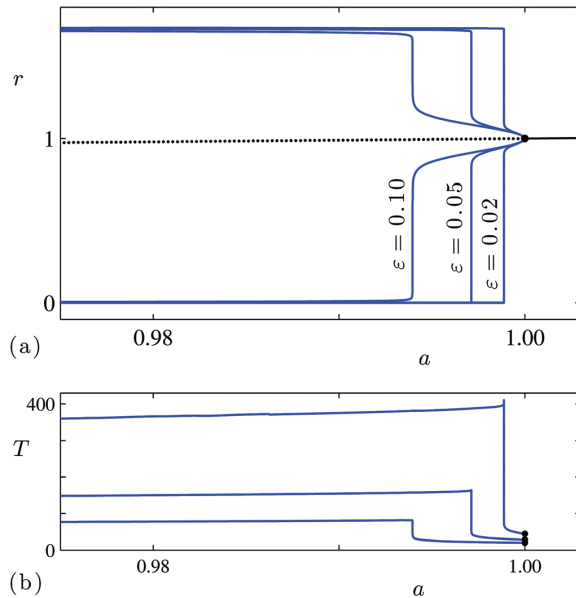


FIG. 4. (Color online) (a) Bifurcation diagram of the  $r-z$  system from Eq. (3) for several values of  $\varepsilon$ . The branch of fixed points undergoes a Hopf bifurcation at  $a=1$ ; this branch is plotted as a solid (dotted) line where it is stable (unstable). Each branch of limit cycles (one per  $\varepsilon$  value) is plotted as two curves, corresponding to the maximum and minimum values of  $r$  over the cycle. (b) The period of the orbits for each of the three values of  $\varepsilon$ . The period at onset is  $T = 2\pi/\sqrt{\varepsilon}$  and is indicated with the  $\bullet$  symbol.

rotations of the periodic orbits from the planar system shown in Fig. 3. The first frequency identified with the tori is fixed at  $\omega$ , while the second frequency varies with  $a$  and is associated with motion in the  $r-z$  cross-section (Fig. 4(b)). The location in  $a$  and abruptness of the torus canard explosion are identical to the planar case for the same  $\varepsilon$ . Near the torus bifurcation, the orbits around the tori are SAO which remain in the neighborhood of  $r=1$ . Beyond the torus canard explosion (i.e., smaller  $a$ ), the orbits around the tori are LAO which include periods of quiescence as the trajectory passes near  $r=0$ .

Therefore, small and large amplitude oscillations in system (3) occur in mutually exclusive ranges of the parameter  $a$ , and as a result this system does not include any MMO. For MMO to exist, one would need a trajectory to alternate between SAO and LAO at a fixed value of  $a$ . In what follows, we show that breaking the rotational symmetry of system (3) generates MMO by creating a region where SAO and LAO coexist, depending on the phase of the orbit.

*Remark:* System (3) is similar to the equations used in Refs. 30 and 31 to model elliptic bursters—i.e., a two dimensional fast-slow system that exhibits canard behavior, trivially extended to three dimensions by rotation about a slow null-cline. The resulting dynamics of a single elliptic burster is consistent with the description presented here for the dynamics of system (3). Those works focus on the synchronization properties of networks of bursters, where the rotational symmetry of the individual burster is effectively broken by phase dependent coupling to the rest of the network.

*Remark:* For orbits on the torus, there is the possibility of resonance between the two frequencies associated with

the motion. In the regime of large  $\omega$ , these are higher order resonances—i.e.,  $\mathcal{O}(\varepsilon^{-1})$ :1—and do not have a noticeable effect on the dynamics. However, these resonances may play an important role in the regime of small  $\omega$ ; see Ref. 39 for a discussion of this effect in the context of a mechanical self-oscillator.

#### IV. THE MAIN THIRD-ORDER SYSTEM AND ITS TORUS CANARDS

In this section, we introduce the main third-order system that we study and show the torus canards that it possesses. As stated in the Introduction, we obtain the main system (1) by adjusting the  $\dot{z}$  equation to shift the  $z$ -null-surface a distance  $b$  in the cartesian  $x$ -direction, thereby breaking the phase invariance of the rotated planar system (3). The equations are

$$\dot{r} = r(z - f(r)), \quad (5a)$$

$$\dot{\theta} = \omega, \quad (5b)$$

$$\dot{z} = \varepsilon \left( a - \sqrt{r^2 - 2rb \cos \theta + b^2} \right), \quad (5c)$$

where  $b > 0$  is the parameter that controls the strength of the symmetry breaking, and we recall that  $f(r) = 2r^3 - 3r^2 + 1$ . In Cartesian coordinates, this system is

$$\dot{x} = x(z - f(\sqrt{x^2 + y^2})) - \omega y, \quad (6a)$$

$$\dot{y} = y(z - f(\sqrt{x^2 + y^2})) + \omega x, \quad (6b)$$

$$\dot{z} = \varepsilon \left( a - \sqrt{(x-b)^2 + y^2} \right). \quad (6c)$$

The vector field is not analytic at  $\{(x, y, z) | x = b, y = 0\}$  due to the branch point of the square root in the  $\dot{z}$  equation, but this does not affect the torus bifurcation or the creation of torus canards which are of interest here. Furthermore, while we focus on a general choice of  $f(r)$  here, one can assume analyticity also at  $r=0$  by choosing  $f(r)$  to be a function of  $r^2$  only. Generalizations of this system that include arbitrary symmetry breaking terms and do not suffer from this branch point are presented in Sec. VII.

Notice that system (5) includes three time scales, because the  $\mathcal{O}(\omega)$  dynamics of the  $\theta$ -variable is now coupled to the fast  $\mathcal{O}(1)$  and slow  $\mathcal{O}(\varepsilon)$  dynamics familiar from the planar case. In the analysis that follows, we focus on the two regimes where  $\omega$  is comparable to either the fast or the slow dynamics. In the former,  $\omega = \mathcal{O}(1)$  so system (5) includes one slow and two fast variables. In the latter,  $\omega = \mathcal{O}(\varepsilon)$  so system (5) includes two slow and one fast variables. We also present numerical results for intermediate values of  $\omega$ .

We begin with a brief description of the wide range of dynamics exhibited by system (5), as shown in Fig. 5. At sufficiently large  $a > 1$ , the system exhibits stable, uniform amplitude spiking at frequency  $\omega$ . As  $a$  decreases, uniform amplitude spiking becomes unstable, and stability is transferred to SAO (Fig. 5(a), where the envelope  $r(t)$  remains close to  $r=1$ ). At different values of  $a$ , the system exhibits LAO (Fig. 5(c), where  $r(t)$  spends some time in the

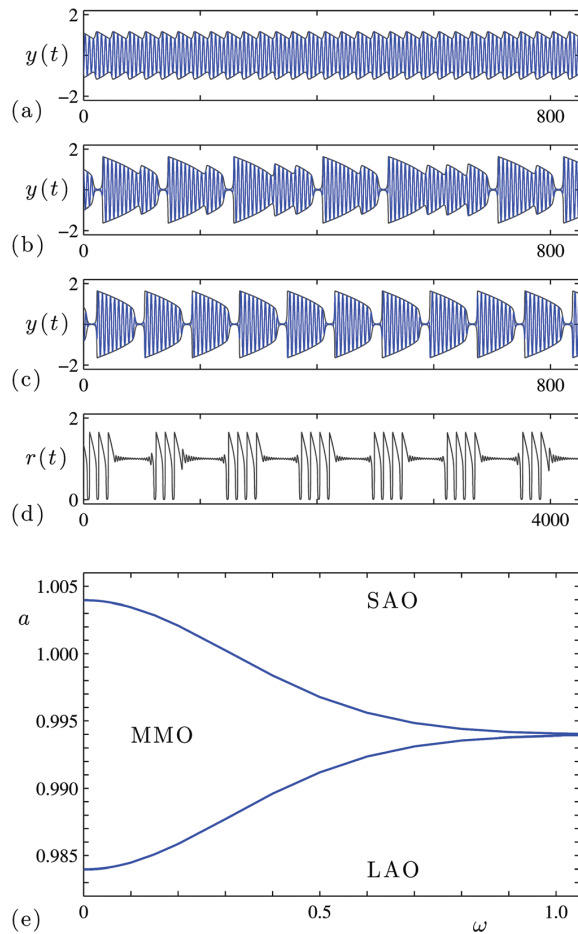


FIG. 5. (Color online) (a–c) Behavior of system (5) at three different values of the parameter  $a$ : (a) SAO, at  $a = 0.9945$ ; (b) MMO, at  $a = 0.99398$ ; (c) LAO, at  $0.9935$ . In each of these panels, the remaining parameters are fixed at  $b = 0.01$ ,  $\varepsilon = 0.1$ ,  $\omega = 0.9$  and the plot includes both  $y(t) = r(t) \sin \theta(t)$  and the envelope  $r(t)$ . (d) MMO at  $a = 0.99398$ ,  $b = 0.01$ ,  $\varepsilon = 0.1$ ,  $\omega = 0.01$ , corresponding to slow rotation. For clarity, only  $r(t)$  is included in this frame. (e) Summary of the dynamics exhibited by system (5), shown in the  $(\omega, a)$  parameter plane at  $b = 0.01$ ,  $\varepsilon = 0.1$ . The boundaries in (e) were computed using the continuation technique outlined in the Remark at the end of Sec. IV.

neighborhood of  $r = 0$ ) and MMO (Fig. 5(b), where the trajectory alternates between large and small amplitude oscillations). As shown in Fig. 5(e), the MMO occur over a range of intermediate  $a$  values between the regions of SAO and LAO, and this range in  $a$  varies with  $\omega$ . The MMO are more robust for small  $\omega$  (i.e., the two slow and one fast regime) but persist for large  $\omega$  (i.e., the one slow two fast regime). In what follows, we show that torus canards are responsible for creating the MMO region.

We now proceed with the analysis of system (5). It is useful to define two surfaces in the three dimensional phase space of this system,

$$\begin{aligned} \mathcal{N}_r &= \{(r, \theta, z) | z = f(r)\}, \\ \mathcal{N}_z &= \{(x, y, z) | a^2 = (x - b)^2 + y^2\}. \end{aligned} \quad (7)$$

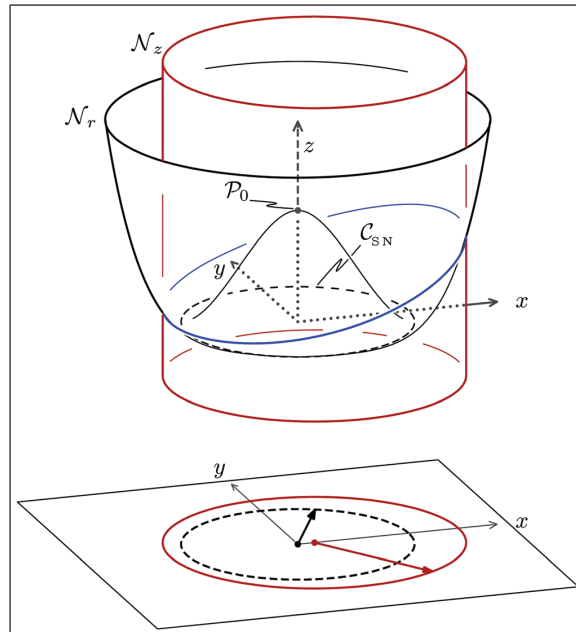


FIG. 6. (Color online) The null-surfaces  $\mathcal{N}_r$  and  $\mathcal{N}_z$  of system (5). The curve  $\mathcal{C}_{SN}$  traces out the local minimum of  $\mathcal{N}_r$ . The point  $\mathcal{P}_0$  is a local maximum of  $\mathcal{N}_r$ . The curve at the intersection of these two null-surfaces ( $\mathcal{N}_r \cap \mathcal{N}_z$ ) is shown for reference. The lower part of the figure shows a projection onto the  $(x, y)$  plane. The projection of  $\mathcal{C}_{SN}$  is a circle of unit radius, centered at the origin. The projection of  $\mathcal{N}_z$  is a circle of radius  $a$ , centered at  $(x, y) = (b, 0)$ . In this figure,  $a = 1.3$  and  $b = 0.2$ .

These are plotted in Fig. 6. The surface  $\mathcal{N}_z$  is the  $z$ -null-surface of Eq. (5). It is a cylinder of radius  $a$  with axis  $\{(x, y, z) | x = b, y = 0\}$ . Inside the cylinder,  $z$  is positive, and outside it is negative. The surface  $\mathcal{N}_r$  is the main branch of the  $r$ -null-surface of Eq. (5)—above the surface  $\dot{r}$  is positive and below it is negative; the other branch of the  $r$ -null-surface is the  $z$ -axis. The curve  $\mathcal{C}_{SN} = \{(r, \theta, z) | r = 1, z = 0\}$  traces out the fold at the local minimum of  $\mathcal{N}_r$ , and the point  $\mathcal{P}_0 = \{(r, \theta, z) | r = 0, z = 1\}$  is a local maximum of this surface.

The surface  $\mathcal{N}_r$ , excluding a small neighborhood of  $\mathcal{C}_{SN}$  and  $\mathcal{P}_0$ , is a normally hyperbolic invariant manifold of system (5) when  $\varepsilon = 0$ , as is  $\mathcal{N}_z$  with a neighborhood of  $\mathcal{P}_0$  excluded. In the remainder of this section, we briefly examine how these manifolds persist for  $0 < \varepsilon \ll 1$ , using Fenichel theory,<sup>21,34</sup> following in particular the presentation of Ref. 35. We exclude small neighborhoods of the ring  $\mathcal{C}_{SN}$  and the point  $\mathcal{P}_0$ , where the manifolds are not normally hyperbolic. We label the different segments of these manifolds according to whether they are attracting or repelling in the fast subsystem, with the subscripts  $a$  and  $r$  denoting attracting and repelling, respectively. Let  $\mathcal{S}_{a,1}^0$  denote the portion of the  $z$ -axis with  $z < 1$ , which is the attracting portion of this critical set, and include the superscript zero to denote  $\varepsilon = 0$ . Let  $\mathcal{S}_{r,1}^0$  be the portion of the  $z$ -axis with  $z > 1$ , which is the repelling portion. Next, let  $\mathcal{S}_{a,2}^0$  denote the attracting portion of the null-cline  $\mathcal{N}_r$ , i.e., that portion with  $r > 1$ , and let  $\mathcal{S}_{r,2}^0$  be that portion with  $0 < r < 1$  which is repelling. So at

$\varepsilon = 0$ , the attracting manifold is  $\mathcal{S}_{a,1}^0 \cup \mathcal{S}_{a,2}^0$ , and the repelling manifold is  $\mathcal{S}_{r,1}^0 \cup \mathcal{S}_{r,2}^0$ .

Each of these normally hyperbolic invariant manifolds persists for sufficiently small  $\varepsilon > 0$  as attracting and repelling manifolds that are invariant under the dynamics of the system (5), as we will now show. We use the superscript  $\varepsilon$  to denote the persistent manifolds. Of course, the  $z$ -axis is clearly also an invariant set of the full system (5), and so the existence of the attracting and repelling manifolds  $\mathcal{S}_{a,1}^\varepsilon$  and  $\mathcal{S}_{r,1}^\varepsilon$ , which coincide with their unperturbed ( $\varepsilon = 0$ ) counterparts, is straightforward. In order to demonstrate the persistence of the surfaces  $\mathcal{S}_{a,2}^0$  and  $\mathcal{S}_{r,2}^0$ , we consider separately the two cases  $\omega = \mathcal{O}(\varepsilon)$  and  $\omega = \mathcal{O}(1)$ . In the regime  $\omega = \mathcal{O}(\varepsilon)$ , the manifolds  $\mathcal{S}_{a,2}^0$  and  $\mathcal{S}_{r,2}^0$  are manifolds of fixed points of the fast system (referred to as critical manifolds) and hence normally hyperbolic invariant manifolds of the full system. The Fenichel theory<sup>21</sup> then applies directly to yield the persistence of these manifolds as slow invariant manifolds, which we label  $\mathcal{S}_{a,2}^\varepsilon$  and  $\mathcal{S}_{r,2}^\varepsilon$ . Moreover, we note that these persistent manifolds are differentially  $\mathcal{O}(\varepsilon)$  close to the critical manifolds.

In the regime of  $\omega = \mathcal{O}(1)$ , the surfaces  $\mathcal{S}_{a,2}^0$  and  $\mathcal{S}_{r,2}^0$  are invariant manifolds foliated by periodic orbits of the fast subsystem. They are also normally hyperbolic invariant manifolds of the full system. The more general Fenichel theory of persistence of normally hyperbolic invariant manifolds<sup>20,21</sup> guarantees the persistence of these manifolds for sufficiently small  $\varepsilon$ . In particular, we use the Fenichel theory presented in Ref. 35 to conclude that the full system possesses invariant manifolds, which we also label  $\mathcal{S}_{a,2}^\varepsilon$  and  $\mathcal{S}_{r,2}^\varepsilon$ , that are differentially  $\mathcal{O}(\varepsilon)$  close to their unperturbed counterparts. Of course, in this regime, the dynamics in the  $\theta$  direction is fast and the dynamics in the  $z$  direction is slow.

In both  $\omega$  regimes,  $\mathcal{S}_{a,2}^\varepsilon$  and  $\mathcal{S}_{r,2}^\varepsilon$  are cylinders topologically, defined over the intervals  $r > 1$  and  $0 < r < 1$ , respectively. Orbits on these invariant manifolds evolve slowly in  $z$ , at an  $\mathcal{O}(\varepsilon)$  rate, and orbits off these invariant manifolds are rapidly attracted to them in forward or backwards time, respectively.

The presence of these manifolds enables us to understand the dynamics of system (5). In fact, the relative dispo-

sitions of these two persistent invariant manifolds (i.e., their global geometry) govern the existence of the torus canards and the varied behavior shown in Fig. 5, as we will now show. First, observe that orbits on  $\mathcal{S}_{a,2}^\varepsilon$  will flow beyond the fold  $\mathcal{C}_{\text{SN}}$  into the regime  $r < 1$  and will typically end up either above or below the other persistent invariant manifold  $\mathcal{S}_{r,2}^\varepsilon$ . Those that lie below will undergo a large amplitude oscillation, jumping to a neighborhood of  $\mathcal{S}_{a,1}^\varepsilon$  and slowly drifting up the  $z$ -axis (Fig. 7, trajectory  $\gamma_1$ ). Those that lie above will undergo a small amplitude oscillation as they quickly move back to larger values of  $r$  (Fig. 7, trajectory  $\gamma_2$ ). Similarly, in backward time, orbits on  $\mathcal{S}_{r,2}^\varepsilon$  will flow past the fold  $\mathcal{C}_{\text{SN}}$  into the regime  $r > 1$ , and end up either above or below  $\mathcal{S}_{a,2}^\varepsilon$  (Fig. 7, trajectories  $\gamma_3$  and  $\gamma_4$ , respectively). We define a *maximal torus canard* as an intersection of  $\mathcal{S}_{a,2}^\varepsilon$  and  $\mathcal{S}_{r,2}^\varepsilon$ . It follows that maximal torus canards are found in pairs, and that they act as separatrices on the two-dimensional persistent invariant manifolds. For example, maximal torus canards separate regions on  $\mathcal{S}_{a,2}^\varepsilon$  where individual trajectories behave qualitatively like  $\gamma_1$  of Fig. 7 from regions where they behave qualitatively like  $\gamma_2$ .

Intersections of the attracting and repelling persistent invariant manifolds clearly play an important role in forming torus canards. To locate and study such intersections, we examine these manifolds as they cross the surface  $\Sigma = \{(r, \theta, z) | r = 1\}$ , a cylinder of unit radius that contains the fold  $\mathcal{C}_{\text{SN}}$  of  $\mathcal{N}_r$ . The phase space plots in Fig. 7 include  $\Sigma$  for reference. Figure 8 shows the manifolds  $\mathcal{S}_{a,2}^\varepsilon$  and  $\mathcal{S}_{r,2}^\varepsilon$  as they cross  $\Sigma$ , plotted in coordinates labelled  $(\theta_\Sigma, z_\Sigma)$  to indicate measurement on  $\Sigma$ . Intuitively, this involves flowing a ring of initial conditions from high up the attracting part of  $\mathcal{N}_r$  forward in time until they cross  $\Sigma$  and likewise for a ring of initial conditions flowed backward in time from the repelling part of  $\mathcal{N}_r$ . In practice, each curve in the figure is traced out by continuation in the boundary condition of an appropriately defined boundary value problem.

The upper panels in Fig. 8 show how the intersections of  $\mathcal{S}_{a,2}^\varepsilon$  and  $\mathcal{S}_{r,2}^\varepsilon$  with  $\Sigma$  vary as the parameter  $a$  changes. At large  $a$  values (Fig. 8(a)),  $\mathcal{S}_{a,2}^\varepsilon$  lies above  $\mathcal{S}_{r,2}^\varepsilon$  for all  $\theta_\Sigma$ , so the persistent manifolds do not intersect and each trajectory from  $\mathcal{S}_{a,2}^\varepsilon$  undergoes a small amplitude oscillation in  $r < 1$ ,

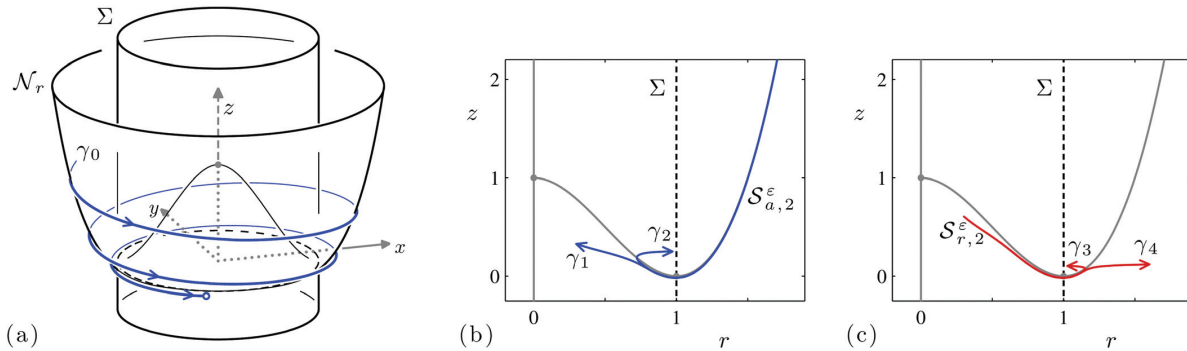


FIG. 7. (Color online) Sketch of trajectories from system (5). (a) The trajectory  $\gamma_0$  from  $\mathcal{S}_{a,2}^\varepsilon$  lies close to  $\mathcal{N}_r$  in  $r > 1$ . The point where it crosses  $\Sigma$  is marked with the  $\circ$  symbol. (b) When such trajectories enter  $r < 1$ , they typically transition to fast motion in  $r$ , either toward small  $r$  (trajectory  $\gamma_1$ ) or large  $r$  (trajectory  $\gamma_2$ ). (c) Trajectories on  $\mathcal{S}_{r,2}^\varepsilon$  enter  $r > 1$  in backward time, then transition to fast motion in  $r$ , either decreasing (trajectory  $\gamma_3$ ) or increasing (trajectory  $\gamma_4$ ). Note that  $\Sigma$  is distinct from the cylindrical null-surface  $\mathcal{N}_z$  included in Fig. 6.

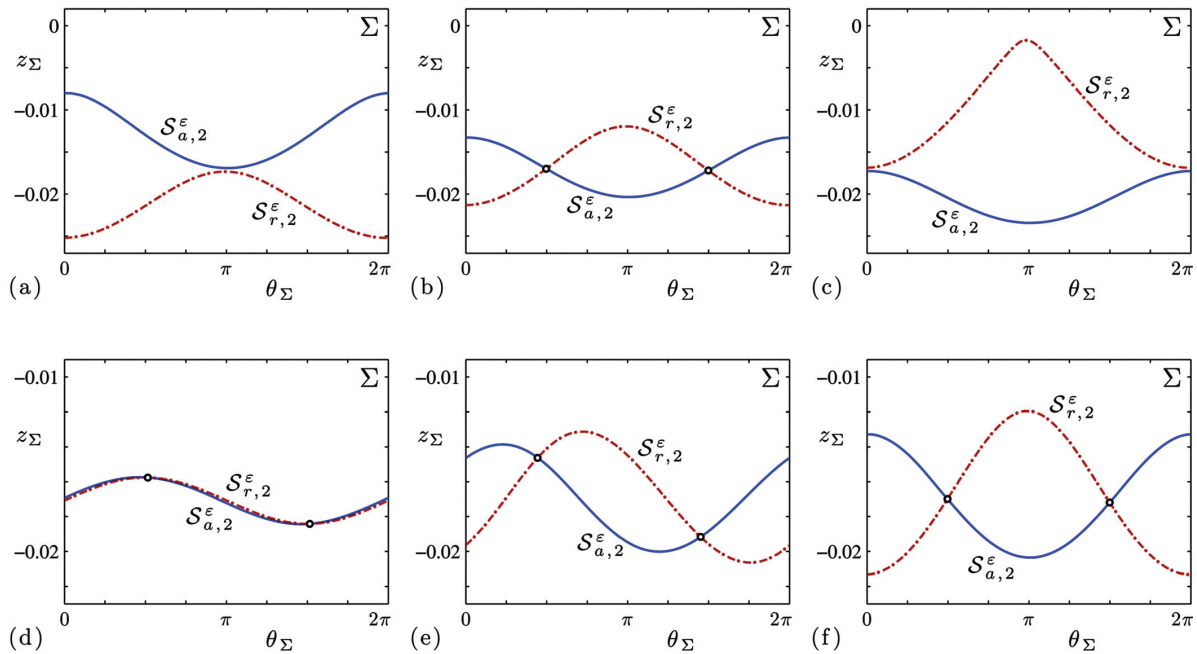


FIG. 8. (Color online) Plots of the manifolds  $\mathcal{S}_{a,2}^\epsilon$  and  $\mathcal{S}_{r,2}^\epsilon$  as they cross the surface  $\Sigma$ , plotted in coordinates  $(\theta_\Sigma, z_\Sigma)$  measured on  $\Sigma$ . The upper panels show the manifolds move through each other as  $a$  varies. (a) At  $a = 1.00448$ ,  $\mathcal{S}_{a,2}^\epsilon$  lies above  $\mathcal{S}_{r,2}^\epsilon$ ; (b) at  $a = 0.99398$ , they intersect; (c) at  $a = 0.98348$ ,  $\mathcal{S}_{a,2}^\epsilon$  lies below  $\mathcal{S}_{r,2}^\epsilon$ . Other parameters in (a–c):  $\omega = 0.01$ ,  $b = 0.01$ ,  $\epsilon = 0.1$ . The lower panels show different regimes for the rotation rate: (d) fast, at  $\omega = 0.9$ ; (e) intermediate, at  $\omega = 0.3$ ; and (f) slow, at  $\omega = 0.01$ . Other parameters in (d–f):  $a = 0.99398$ ,  $b = 0.01$ ,  $\epsilon = 0.1$ . Intersections are indicated in each panel with the  $\circ$  symbol.

similar to  $\gamma_2$  from Fig. 7. Decreasing the parameter  $a$  causes  $\mathcal{S}_{a,2}^\epsilon$  to move down and  $\mathcal{S}_{r,2}^\epsilon$  to move up in  $z_\Sigma$ , so at smaller  $a$  values (Fig. 8(c)),  $\mathcal{S}_{a,2}^\epsilon$  lies below  $\mathcal{S}_{r,2}^\epsilon$  for all  $\theta_\Sigma$ . In this case, each trajectory from  $\mathcal{S}_{a,2}^\epsilon$  undergoes a large amplitude oscillation in  $r < 1$ , similar to  $\gamma_1$  from Fig. 7. At the intermediate value of  $a$  shown in Fig. 8(b) the manifolds intersect, so both large and small amplitude orbits are possible, depending on the initial condition. The lower panels in Fig. 8 show how the manifolds deform as  $\omega$  varies. At the particular  $a$  value used in these panels, the intersection of  $\mathcal{S}_{a,2}^\epsilon$  and  $\mathcal{S}_{r,2}^\epsilon$  persists from small  $\omega$  (Fig. 8(f)) well into the regime of large  $\omega$  (Fig. 8(d)). As  $\omega$  increases, the  $\theta_\Sigma$  variation of the two manifolds becomes nearly identical and so the intersection becomes less robust to changes in the parameter  $a$  (which shift  $\mathcal{S}_{r,2}^\epsilon$  and  $\mathcal{S}_{a,2}^\epsilon$  in opposite directions in  $z_\Sigma$ ).

The persistence of the intersections of  $\mathcal{S}_{a,2}^\epsilon$  and  $\mathcal{S}_{r,2}^\epsilon$  is in part a consequence of simple geometry. In the two-dimensional planar system described in Sec. III, the attracting and repelling slow manifolds were each one-dimensional invariant sets, so their intersection occurred at a unique value of the parameter  $a$ . In the three-dimensional system considered here,  $\mathcal{S}_{a,2}^\epsilon$  and  $\mathcal{S}_{r,2}^\epsilon$  are each two-dimensional invariant surfaces. The one-dimensional intersections of such surfaces are structurally stable and therefore persist over a range of  $a$  values.

The maximal torus canards lie along the intersections of  $\mathcal{S}_{a,2}^\epsilon$  and  $\mathcal{S}_{r,2}^\epsilon$ . Torus canards occur near these intersections where the separation between the manifolds is necessarily small. Restricting our attention to trajectories on  $\mathcal{S}_{a,2}^\epsilon$ , this means that there is a strip of torus canard trajectories surrounding each maximal torus canard. When  $\omega$  is small (as in

Fig. 8(b)), this strip of torus canards is narrow, including only a small fraction of the trajectories on  $\mathcal{S}_{a,2}^\epsilon$ . When  $\omega$  is larger (as in Fig. 8(d)), the strip of torus canards is broader and may grow to include the entire surface.

The intersection of  $\mathcal{S}_{a,2}^\epsilon$  and  $\mathcal{S}_{r,2}^\epsilon$  also implies the existence of MMO. A single MMO trajectory cycles through  $\Sigma$  many times, and for any nonzero  $\omega$ , the value of  $\theta_\Sigma$  will in general change with each cycle. A detailed study of the sequence of  $\theta_\Sigma$  values generated by the global return map  $\Sigma \rightarrow \Sigma$  is beyond the scope of this article. However, the global return does appear to mix the two ranges of  $\theta_\Sigma$  that lie on either side of the maximal torus canards. We find numerically that the  $\theta_\Sigma$  sequence almost always includes  $\theta_\Sigma$  values where  $\mathcal{S}_{a,2}^\epsilon$  lie above  $\mathcal{S}_{r,2}^\epsilon$ , as well as values where  $\mathcal{S}_{a,2}^\epsilon$  lies below  $\mathcal{S}_{r,2}^\epsilon$ . This explains why the range over which the persistent invariant manifolds  $\mathcal{S}_{a,2}^\epsilon$  and  $\mathcal{S}_{r,2}^\epsilon$  intersect (and hence the range over which torus canards occur) matches exactly the range over which MMO are observed in Fig. 5(e). In the regime of small  $\omega$ , MMO consist of many SAO followed by many LAO due to the fact that the angle  $\theta_\Sigma$  changes by a small amount each cycle (Fig. 5(d)). When  $\omega$  is larger, the MMO transitions more frequently between large and small amplitude oscillations (Fig. 5(b)).

Note that the maximal torus canards are typically not global attractors of the dynamics of the full system (5) and need not appear in the MMO sequence. Nevertheless, the maximal torus canards allow  $\mathcal{S}_{a,2}^\epsilon$  to simultaneously include both SAO and LAO orbits, thereby playing a crucial role in guiding the long time dynamics of the system and creating MMO.

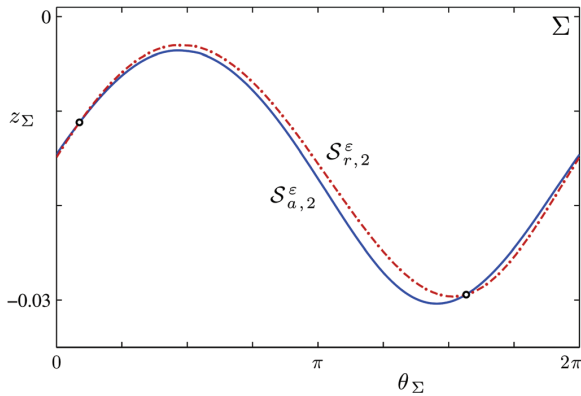


FIG. 9. (Color online) Similar to Fig. 8, but at a larger value of  $b$ . Parameters:  $a = 0.9955$ ,  $b = 0.1$ ,  $\varepsilon = 0.1$ ,  $\omega = 0.9$ .

Clearly, the magnitude of  $\omega$  is particularly important in determining how robust the torus canard phenomenon is to changes in parameters. We analyze the cases of large and small  $\omega$  in Secs. V and VI, confirming the numerical results about the persistent invariant manifolds, their intersections, and their separation.

*Remark:* We have chosen to use the cylinder  $\{r = 1\}$  as our cross-section  $\Sigma$  in the numerical simulations. As a result, there are threshold values of  $b$  (depending on  $a$  and  $\omega$ ) such that the SAO and LAO in the numerical simulations will hit the cross-section only for values of  $b$  below the threshold. For example, in Fig. 9, we show the images of  $S_{a,2}^\varepsilon$  and  $S_{r,2}^\varepsilon$  on  $\Sigma$  for a value of  $b$  that is an order of magnitude larger than that used in Fig. 8 and that is just below the threshold. To observe the dynamics of the SAO, LAO, and MMO for larger values of  $b$  (with the other parameters fixed), one would need to use a different, more complicated cross-section that is tailored to the shape and amplitude of the symmetry-breaking term. In this sense, the threshold is artificial. We do not pursue other choices of cross-sections here.

*Remark:* The above description focuses on locating the maximal torus canards by tracing out the manifolds  $S_{a,2}^\varepsilon$  and  $S_{r,2}^\varepsilon$ , then searching for their intersections. The maximal torus canards can also be found directly as solutions to a boundary value problem, where the boundaries lie far up the attracting and repelling parts of  $\mathcal{N}_r$ . Numerical continuation of the maximal torus canards provides an efficient way to compute several important properties of these trajectories. For example, the tangencies between  $S_{a,2}^\varepsilon$  and  $S_{r,2}^\varepsilon$  correspond to saddle-node bifurcations of the branch of maximal torus canards. The boundaries of the MMO region in Fig. 5(e) were computed directly in AUTO by continuation of these saddle-node bifurcations in two parameters,  $a$  and  $\omega$ .

### V. FAST ROTATION—AVERAGING FOR LARGE $\omega$

In this section, we analyze the system (5) for large  $\omega$  using averaging. This corresponds to the regime in which system (5) includes one slow and two fast variables. We show that the system includes a periodic orbit which undergoes a torus bifurcation at

$$a \approx 1 + b^2/4. \tag{8}$$

This torus bifurcation plays a similar role in the creation of torus canards as the Hopf bifurcation in the planar case. We employ the method of averaging<sup>28,45</sup> in the regime of large  $\omega$  to establish this basic result about the torus bifurcation. We limit the analysis here to the leading order averaging, and then, at the end of this section, comment on higher order effects. We present numerical evidence that the higher order effects are not crucial for the values of  $b$  considered here.

We define  $\theta_0 = \theta(0)$ , so the  $\dot{\theta}$  component of this system is trivially solved by  $\theta(t) = \omega t + \theta_0$ . The  $z$ -component of the vector field is periodic with period  $2\pi/\omega$ . We use  $\bar{z}$  to denote this variable in the averaged system, and let  $z = \bar{z} + \delta\zeta(r, \bar{z}, t)$  with  $\delta = \mathcal{O}(\varepsilon b)$ . Then,

$$\dot{z} = \dot{\bar{z}} + \delta \frac{\partial \zeta}{\partial t} + \delta \frac{\partial \zeta}{\partial r} \dot{r} + \delta \frac{\partial \zeta}{\partial \bar{z}} \dot{\bar{z}} \tag{9}$$

and

$$\begin{aligned} \dot{\bar{z}} &= \left(1 + \delta \frac{\partial \zeta}{\partial \bar{z}}\right)^{-1} \left(\dot{z} - \delta \frac{\partial \zeta}{\partial r} \dot{r} - \delta \frac{\partial \zeta}{\partial t}\right) = \left(1 + \delta \frac{\partial \zeta}{\partial \bar{z}}\right)^{-1} \\ &\times \left[\varepsilon \left(a - \sqrt{r^2 - 2rb \cos(\omega t + \theta_0) + b^2}\right) - \delta \frac{\partial \zeta}{\partial r} \dot{r} - \delta \frac{\partial \zeta}{\partial t}\right]. \end{aligned} \tag{10}$$

We will choose the function  $\zeta$  so that the oscillatory part of the square root is canceled from the above equation. With this goal in mind, it is natural to choose  $\delta = \varepsilon b$  instead of the weaker assumption that  $\delta = \mathcal{O}(\varepsilon b)$ . Thus,

$$\begin{aligned} \dot{\bar{z}} &= \varepsilon \left(1 + \varepsilon b \frac{\partial \zeta}{\partial \bar{z}}\right)^{-1} \\ &\times \left(a - \sqrt{r^2 - 2rb \cos(\omega t + \theta_0) + b^2} - b \frac{\partial \zeta}{\partial r} \dot{r} - b \frac{\partial \zeta}{\partial t}\right). \end{aligned} \tag{11}$$

Next, we show that  $\dot{r} = \mathcal{O}(\varepsilon)$  along the trajectories of interest. In particular, the initial conditions of these trajectories satisfy either  $r(0) > 1$  or  $0 < r(0) < 1$ . Provided the solution is outside a neighborhood of the fold  $\mathcal{C}_{\text{SN}}$ , it follows from Fenichel theory that the orbit will be exponentially attracted to  $S_{a,2}^\varepsilon$  in forward time or  $S_{r,2}^\varepsilon$  in backward time, and in both cases  $\dot{r} = \mathcal{O}(\varepsilon)$  to leading order. Therefore, for orbits for which  $r(t)$  stays outside of a small neighborhood of  $r = 1$ , Eq. (11) simplifies to

$$\begin{aligned} \dot{\bar{z}} &= \varepsilon \left(1 + \varepsilon b \frac{\partial \zeta}{\partial \bar{z}}\right)^{-1} \\ &\times \left(a - \sqrt{r^2 - 2rb \cos(\omega t + \theta_0) + b^2} - b \frac{\partial \zeta}{\partial t}\right) + \mathcal{O}(\varepsilon^2 b). \end{aligned} \tag{12}$$

We separate the square root into a sum of its average and oscillatory parts using the identity

$$\sqrt{r^2 - 2rb \cos(\omega t + \theta_0) + b^2} = \frac{(r-b)}{\pi} E\left(\pi, \frac{-4br}{(r-b)^2}\right) + \left[ \sqrt{r^2 - 2rb \cos(\omega t + \theta_0) + b^2} - \frac{(r-b)}{\pi} E\left(\pi, \frac{-4br}{(r-b)^2}\right) \right],$$

where  $E(\cdot, \cdot)$  is the incomplete elliptic integral of the second kind.<sup>10</sup> Clearly, if we choose  $\zeta$  such that

$$\frac{\partial \zeta}{\partial t} = -\frac{1}{b} \left[ \sqrt{r^2 - 2rb \cos(\omega t + \theta_0) + b^2} - \frac{(r-b)}{\pi} E\left(\pi, \frac{-4br}{(r-b)^2}\right) \right], \tag{13}$$

then we see that  $\zeta$  is independent of  $\bar{z}$  so that  $\partial \zeta / \partial \bar{z} = 0$  and Eq. (12) for  $\bar{z}$  reduces to

$$\dot{\bar{z}} = \varepsilon \left[ a - \frac{(r-b)}{\pi} E\left(\pi, \frac{-4br}{(r-b)^2}\right) \right] + \mathcal{O}(\varepsilon^2 b). \tag{14}$$

Equation (14) is the leading order averaged equation. For the values of  $b$  shown in Fig. 10, the leading order term dominates and the remainder is second order in  $\varepsilon$  and also linearly proportional to  $b$ .

The main result (8) about the torus bifurcation is now at hand. In particular, we expand the incomplete elliptic integral in powers of  $b$  and find

$$\dot{\bar{z}} = \varepsilon \left( a - r - \frac{b^2}{4r} \right) + \mathcal{O}(\varepsilon b^3, \varepsilon^2 b). \tag{15}$$

Now, since the fold of  $\mathcal{N}_r$  is at  $r = 1$ , it follows that the torus bifurcation should occur when  $a \approx 1 + b^2/4$ , which establishes Eq. (8). This parabola is shown in Fig. 10 and fits well to the data points obtained from numerically computed torus bifurcations.

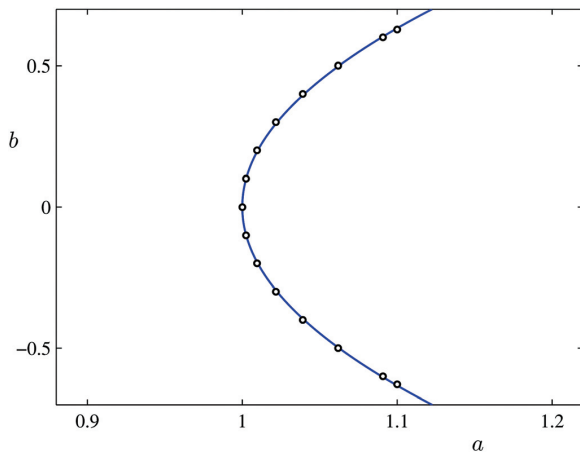


FIG. 10. (Color online) Location of the torus bifurcation in system (5), plotted in the  $(a, b)$  parameter plane. Exact values for  $\omega = 1$  and  $\varepsilon = 0.1$  are indicated with the  $\circ$  symbol and were determined at several fixed  $b$  values by numerical continuation of periodic solutions in the parameter  $a$ . The approximation (8), derived from the leading order averaging, is plotted as a solid curve.

For each value of  $b$  shown in Fig. 10, torus canards exist for a small interval of  $a$  values just below the torus bifurcation. While the first-order averaging is insufficiently sensitive to find these intervals analytically, they may be found (and we found them) numerically. They are narrow intervals and get narrower as  $\omega$  gets larger (data not shown).

*Remark:* In using Eq. (15) in the limit that  $b \rightarrow 0$ , one has to exercise care with how small  $b$  is relative to  $\varepsilon$ , as one of the remainder terms eventually becomes more important than the  $b^2$  term in parentheses. We do not pursue this small correction for very small values of  $b$  here.

*Remark:* It is important to note that the assumption made above that  $\dot{r} = \mathcal{O}(\varepsilon)$  only holds outside a small neighborhood of the fold  $\mathcal{C}_{\text{SN}}$ , because the Fenichel theory only applies outside this neighborhood. Nevertheless, the orbits we study here briefly pass through this neighborhood. Hence, to make the above averaging fully rigorous, one needs to use the theory of Ref. 42 to determine the size, which is  $\mathcal{O}(\varepsilon^p)$  for some  $0 < p < 1$  of  $\dot{r}$  in this brief interval. Also, it may be possible to get a much sharper bound on the closeness of the images on  $\Sigma$  in the regime of fast rotations (Fig. 8(d)) by using the ideas in Ref. 41.

**VI. SLOW ROTATION—BLOW-UP FOR SMALL  $\omega$**

In this section, we use geometric desingularization<sup>16</sup> to understand the dynamics in the slow rotation regime. This corresponds to the regime in which system (5) includes two slow and one fast variables. The geometric desingularization method, which is also known as the blow-up method, enables one to naturally extend geometric singular perturbation theory<sup>21,34</sup> to fast-slow problems with relaxation oscillations to overcome the loss of hyperbolicity at fold points.<sup>17,37,38</sup> As mentioned in Sec. IV, the MMO in system (5) become more robust when  $\theta$  is a slowly varying parameter—i.e., they occur over a wider range in the parameter  $a$  for each fixed value of  $b > 0$ . To better understand the dynamics in this regime, we assume  $\omega = \varepsilon \bar{\omega}$ , where  $\bar{\omega}$  is  $\mathcal{O}(1)$  with respect to  $\varepsilon$  and adopt the blow-up method of Refs. 16, 17, and 49. In particular, we blow up the ring  $\mathcal{C}_{\text{SN}}$  along the fold of the  $r$ -null-surface  $\mathcal{N}_r$ .

Since we are concerned with dynamics near  $r = 1$  (recall that  $\mathcal{C}_{\text{SN}} = \{(r, \theta, z) | r = 1, z = 0\}$ ), we make a change of variables  $s = r - 1$  and introduce the new parameter  $\lambda = a - 1$ . After expanding in powers of  $b$ , we find that system (5) becomes

$$\dot{s} = z(1 + s) - 3s^2 - 5s^3 - 2s^4, \tag{16a}$$

$$\dot{\theta} = \varepsilon \bar{\omega}, \tag{16b}$$

$$\dot{z} = \varepsilon(g(s, \theta, \lambda, b) + h(s, \theta, b) + \mathcal{O}(b^3)), \tag{16c}$$

$$\dot{\varepsilon} = 0, \tag{16d}$$

$$\dot{\lambda} = 0, \tag{16e}$$

$$\dot{b} = 0, \tag{16f}$$

where

$$g(s, \theta, \lambda, b) = -s + \lambda + b \cos \theta, \tag{17a}$$

$$h(s, \theta, b) = -b^2 \frac{\sin^2 \theta}{2(1+s)}. \tag{17b}$$

The blow-up is given by

$$s = \bar{\rho}\bar{s}, \quad z = \bar{\rho}^2\bar{z}, \quad \varepsilon = \bar{\rho}^2\bar{\varepsilon}, \quad \lambda = \bar{\rho}\bar{\lambda}, \quad b = \bar{\rho}\bar{b}, \tag{18}$$

which defines a map

$$\Phi : S^5 \times [0, \delta] \times S^1 \rightarrow \mathbb{R}^3 \times \mathbb{R} \times \mathbb{R} \times \mathbb{R} \tag{19}$$

$$(\bar{s}, \bar{z}, \bar{\varepsilon}, \bar{\lambda}, \bar{b}, \bar{\rho}, \theta) \mapsto (r, \theta, z, \varepsilon, \lambda, b).$$

The transformation Eq. (18) blows up the ring  $C_{sn}$  into a cylinder, where the variable  $\theta$  is unaltered. We include both the coordinates and the parameters in the blow-up because we want to locate the maximal torus canards and also predict how they vary with the parameters.

To analyze the blown-up dynamics, we will look at the charts  $K_1$  and  $K_2$  that correspond, respectively, to setting  $\bar{z} = 1$  and  $\bar{\varepsilon} = 1$ ,

$$K_1 : s = \rho_1 s_1, \quad z = \rho_1^2, \quad \varepsilon = \rho_1^2 \varepsilon_1, \quad \lambda = \rho_1 \lambda_1, \quad b = \rho_1 b_1, \tag{20}$$

$$K_2 : s = \rho_2 s_2, \quad z = \rho_2^2 z_2, \quad \varepsilon = \rho_2^2, \quad \lambda = \rho_2 \lambda_2, \quad b = \rho_2 b_2. \tag{21}$$

The chart  $K_1$  is the entry and exit chart, which we will use to study how orbits enter and exit a neighborhood of  $C_{sn}$ . The chart  $K_2$  is the rescaling chart, which we will use to analyze the dynamics of orbits as they pass through the neighborhood of  $C_{sn}$ .

The change of coordinates  $\kappa_{12}$  from  $K_1$  to  $K_2$  is given by

$$s_2 = s_1 \varepsilon_1^{-1/2}, \quad z_2 = \varepsilon_1^{-1}, \quad \lambda_2 = \lambda_1 \varepsilon_1^{-1/2}, \quad b_2 = b_1 \varepsilon_1^{-1/2}, \tag{22}$$

and  $\kappa_{12}^{-1}$  is given by

$$s_1 = s_2 z_2^{-1/2}, \quad \varepsilon_1 = z_2^{-1}, \quad \lambda_1 = \lambda_2 z_2^{-1/2}, \quad b_1 = b_2 z_2^{-1/2}. \tag{23}$$

**A. Dynamics in the chart  $K_1$**

This chart is used to analyze the dynamics around the entry into and exit from the fold region. After rescaling time by a factor of  $\rho_1$ , the equations of motion in this chart are

$$\dot{s}_1 = 1 + \rho_1 s_1 - 3s_1^2 - \frac{1}{2} s_1 \varepsilon_1 (g + \rho_1 h) - 5\rho_1 s_1^3 - 2\rho_1^2 s_1^4, \tag{24a}$$

$$\dot{\theta} = \rho_1 \varepsilon_1 \tilde{\omega}, \tag{24b}$$

$$\dot{\varepsilon}_1 = -\varepsilon_1^2 (g + \rho_1 h) + \mathcal{O}(\rho_1^2), \tag{24c}$$

$$\dot{\rho}_1 = \frac{1}{2} \rho_1 \varepsilon_1 (g + \rho_1 h) + \mathcal{O}(\rho_1^3), \tag{24d}$$

$$\dot{\lambda}_1 = -\frac{1}{2} \lambda_1 \varepsilon_1 (g + \rho_1 h) + \mathcal{O}(\rho_1^2), \tag{24e}$$

$$\dot{b}_1 = -\frac{1}{2} b_1 \varepsilon_1 (g + \rho_1 h) + \mathcal{O}(\rho_1^2), \tag{24f}$$

where  $g = g(s_1, \theta, \lambda_1, b_1)$  and  $h = h(\rho_1 s_1, \theta, b_1)$ . In this chart, we have invariant hypersurfaces corresponding to each of  $\varepsilon_1 = 0$ ,  $\rho_1 = 0$ ,  $\lambda_1 = 0$ , and  $b_1 = 0$ ; in the first two of these surfaces, any hypersurface  $\theta = \theta_0 \in S^1$  is also invariant. The intersection of all these hypersurfaces is an invariant line,

$$\ell_1 = \{(s_1, \theta, \varepsilon_1, \rho_1, \lambda_1, b_1) | \theta = \theta_0, \varepsilon_1 = 0, \rho_1 = 0, \lambda_1 = 0, b_1 = 0\}.$$

This line has two equilibria,  $p_a = (1/\sqrt{3}, \theta_0, 0, 0, 0, 0)$  and  $p_r = (-1/\sqrt{3}, \theta_0, 0, 0, 0, 0)$ ; the former is attracting (on the line) and the latter is repelling. The point  $p_a$  has one stable eigenvector in the  $s$  direction and 5 zero eigenvalues in the directions of  $\theta$ ,  $\rho$ ,  $\lambda$ ,  $b$ , and  $s/12\sqrt{3} + \varepsilon$ . The point  $p_r$  has one unstable eigenvector in the  $s$  direction and 5 zero eigenvalues in the directions of  $\theta$ ,  $\rho$ ,  $\lambda$ ,  $b$ , and  $-s/12\sqrt{3} - \varepsilon$ . The normally hyperbolic invariant manifold  $S_{a,2}^0$  connects directly to  $p_a$ . For small values of  $\varepsilon > 0$ , orbits on the persistent invariant manifold  $S_{a,2}^\varepsilon$  enter the neighborhood of  $C_{sn}$  near  $p_a$ . Similarly, the normally hyperbolic invariant manifold  $S_{r,2}^0$  connects to  $p_r$ , and for small  $\varepsilon > 0$ , orbits on the persistent invariant manifold  $S_{r,2}^\varepsilon$  enter in backward time near  $p_r$ .

**B. Dynamics in the chart  $K_2$**

This chart is used to analyze the flow from the point  $p_a$  to the point  $p_r$ —i.e., the flow through the blow-up region. After rescaling time by a factor of  $\rho_2$ , the dynamics here is

$$\dot{s}_2 = z_2(1 + \rho_2 s_2) - 3s_2^2 - 5\rho_2 s_2^3 - 2\rho_2^2 s_2^4, \tag{25a}$$

$$\dot{\theta} = \rho_2 \tilde{\omega}, \tag{25b}$$

$$\dot{z}_2 = g + \rho_2 h, \tag{25c}$$

$$\dot{\rho}_2 = 0, \tag{25d}$$

$$\dot{\lambda}_2 = 0, \tag{25e}$$

$$\dot{b}_2 = 0, \tag{25f}$$

where  $g = g(s_2, \theta, \lambda_2, b_2)$  and  $h = h(\rho_2 s_2, \theta, b_2)$ . In the invariant surface  $\rho_2 = 0$ , we have

$$\dot{s}_2 = z_2 - 3s_2^2, \tag{26a}$$

$$\dot{z}_2 = -s_2 + \lambda_2 + b_2 \cos \theta, \tag{26b}$$

where  $\theta$ ,  $\lambda_2$ , and  $b_2$  are fixed parameters. If  $|\lambda_2| < |b_2|$ , then for  $\theta = \pm \cos^{-1}(-\lambda_2/b_2)$ , we have

$$\dot{s}_2 = z_2 - 3s_2^2, \tag{27a}$$

$$\dot{z}_2 = -s_2, \tag{27b}$$

which is Hamiltonian with

$$H = \frac{1}{18} e^{-6z_2} \left( 3z_2 - 9s_2^2 + \frac{1}{2} \right), \tag{28a}$$

$$\dot{s}_2 = -e^{6z_2} \frac{\partial H}{\partial z_2}, \tag{28b}$$

$$\dot{z}_2 = e^{6z_2} \frac{\partial H}{\partial s_2}. \tag{28c}$$

The curve  $\Gamma(t) = (s_{2,\Gamma}(t), z_{2,\Gamma}(t)) = (t, 3t^2 - 1/6)$  corresponding to  $H=0$  separates periodic orbits from unbounded solutions and corresponds to the graph of

$$z_2 = 3s_2^2 - \frac{1}{6}. \tag{29}$$

After multiplying this equation by  $\varepsilon_1$ , we can use Eq. (23) to transfer this orbit to chart  $K_1$ ,

$$1 = 3s_1^2 - \frac{1}{6} \varepsilon_1. \tag{30}$$

As  $z_2 \rightarrow \infty$ , we have  $\varepsilon_1 \rightarrow 0$ , and so  $s_1 \rightarrow \pm 1/\sqrt{3}$  along  $\Gamma$ . We also have  $\lambda_1 \rightarrow 0$ ,  $b_1 \rightarrow 0$ , and  $\rho_1 = \rho_2 z_2^{1/2} \equiv 0$  along  $\Gamma$ , so the endpoints of the curve are  $p_a$  and  $p_r$ . Moreover, implicit differentiation yields

$$0 = 6s_1 ds_1 - \frac{1}{6} d\varepsilon_1, \tag{31}$$

so along  $\Gamma$  we have

$$\frac{ds_1}{d\varepsilon_1} = \pm \frac{1}{12\sqrt{3}}. \tag{32}$$

Thus,  $\Gamma$  lies on the center manifolds of both  $p_a$  and  $p_r$  and connects the two points.

**C. Perturbation from the singular limit**

In this section, we use the Melnikov approach employed by Ref. 37 to show that the connection  $\Gamma$  from  $p_a$  to  $p_r$  breaks for  $\varepsilon \neq 0$  and that the intersection of the center manifolds of  $p_a$  and  $p_r$  is transverse. We then use the transversality to compute the first order approximation of the parameter values required to produce such intersections, which correspond to maximal torus canards.

We first define a distance function  $\mathcal{D}(\rho_2, \lambda_2, b_2)$  that uses the value of the Hamiltonian to measure the distance between a trajectory followed from  $p_a$  in forward time and a trajectory followed from  $p_r$  in backward time. Applying Proposition 3.5 of Ref. 37 to our system, we have

$$\mathcal{D}(\rho_2, \lambda_2, b_2) = d_\rho \rho_2 + d_\lambda \lambda_2 + d_b b_2 + d_{\rho\rho} \rho_2^2 + \mathcal{O}(3), \tag{33}$$

where the coefficients of the linear terms are

$$d_\rho = \int_{-\infty}^{\infty} \nabla H(\Gamma(t)) \cdot \begin{bmatrix} z_{2,\Gamma} s_{2,\Gamma} - 5s_{2,\Gamma}^3 \\ 0 \end{bmatrix} dt, \tag{34a}$$

$$d_\lambda = \int_{-\infty}^{\infty} \nabla H(\Gamma(t)) \cdot \begin{bmatrix} 0 \\ 1 \end{bmatrix} dt, \tag{34b}$$

$$d_b = \int_{-\infty}^{\infty} \nabla H(\Gamma(t)) \cdot \begin{bmatrix} 0 \\ \cos \theta \end{bmatrix} dt. \tag{34c}$$

Note that in each integral  $\nabla H$  is dotted with the first-order term from the corresponding Taylor series, with each of the

other parameters being fixed at zero. Also,  $\theta$  is a constant in the last equation, as is consistent to leading order. Using

$$\nabla H(\Gamma(t)) = e^{-6z_{2,\Gamma}} \begin{bmatrix} -s_{2,\Gamma} \\ -(z_{2,\Gamma} - 3s_{2,\Gamma}^2) \end{bmatrix} = e^{1-18t^2} \begin{pmatrix} -t \\ 1/6 \end{pmatrix}, \tag{35}$$

we have

$$d_\rho = \int_{-\infty}^{\infty} e^{1-18t^2} \left( \frac{t^2}{6} + 2t^4 \right) dt = \frac{e\sqrt{2\pi}}{648}, \tag{36a}$$

$$d_\lambda = \int_{-\infty}^{\infty} e^{1-18t^2} \left( \frac{1}{6} \right) dt = \frac{e\sqrt{2\pi}}{36}, \tag{36b}$$

$$d_b = \int_{-\infty}^{\infty} e^{1-18t^2} \left( \frac{\cos \theta}{6} \right) dt = \frac{e\sqrt{2\pi}}{36} \cos \theta. \tag{36c}$$

At higher order, we find

$$d_{\rho\rho} = 2 \int_{-\infty}^{\infty} e^{-6z_{2,\Gamma}} s_{2,\Gamma}^5 dt = 2 \int_{-\infty}^{\infty} e^{1-18t^2} (t^5) dt = 0, \tag{37}$$

and the dominant term of the  $\mathcal{O}(3)$  corrections in Eq. (33) is  $\mathcal{O}(\rho_2 b_2^2)$ .

Applying the condition  $\mathcal{D}(\rho_2, \lambda_2, b_2) = 0$  to locate the intersections, we find

$$\frac{\rho_2}{18} + \lambda_2 + b_2 \cos \theta = \mathcal{O}(\rho_2 b_2^2). \tag{38}$$

Since  $\rho_2 = \varepsilon^{1/2}$ ,  $\lambda_2 = \lambda \varepsilon^{-1/2}$ , and  $b_2 = b \varepsilon^{-1/2}$ , we have

$$\frac{1}{18} \varepsilon + \lambda + b \cos \theta = \mathcal{O}(b^2). \tag{39}$$

Therefore, in terms of the original parameter  $a$ , maximal torus canards occur at

$$a = 1 - \frac{\varepsilon}{18} - b \cos \theta + \mathcal{O}(b^2). \tag{40}$$

We require  $b \ll \varepsilon^{1/2}$  for the remainder to be higher order. These results coincide with those from Ref. 37 in the case  $b=0$ . For  $b \neq 0$  and small  $\omega$ , the relation in Eq. (40) can be used to show that, to leading order, maximal torus canards persist over a range in  $a$  of size  $2b$ . This matches the numerical results presented in the upper panels of Fig. 8. Moreover, for any value of  $a$  within this range, Eq. (40) can be used to calculate  $\theta_\Sigma$  for the intersections of the persistent invariant manifolds on  $\Sigma$ .

We note that the variable  $\theta$  is not included in the blow-up because we want to consider it over the entire range of values on  $S^1$ . Nevertheless, we can still examine its dynamics in the new variables and time-scale used in the blow-up and we get  $\dot{\theta} = \bar{\rho} \varepsilon \omega$ . In general, if  $\dot{\theta} = \varepsilon^\alpha \omega$  then in the blow-up we have  $\dot{\theta} = \bar{\rho}^{2\alpha-1} \varepsilon^\alpha \omega$ . Since the case  $\bar{\rho} = 0$  is important for considering the singular limit of the blow-up, this suggests that  $\alpha = 1/2$  is a critical value in this model, and that  $\dot{\theta} = \varepsilon^{1/2}$  may correspond to a bifurcation in the behavior of this model. In fact, the above analysis carries over for  $\dot{\theta} = \varepsilon^\alpha \omega$  with  $\alpha > 1/2$ , but for  $\alpha < 1/2$ , one is already closer to the fast rotation regime. This is consistent with the

observation in Sec. III that the two frequencies associated with the tori at onset (at least when  $b=0$ ) are  $\omega$  and  $\varepsilon^{1/2}$ , confirming the intuition that the large and small regimes of  $\omega$  should be measured relative to a  $\varepsilon^{1/2}$  frequency scale.

*Remark:* The perturbation theory of Ref. 37, with its Melnikov function  $\mathcal{D}$ , is developed in the context of small-amplitude autonomous perturbations. As noted above, we have used it here for system (5) under the assumption that  $\theta$  is a constant, so that the perturbation is autonomous. We now show briefly that the time-dependence of  $\theta$  leads to higher order terms. In this respect, we first observe that the dominant term in Eq. (25c) is  $b_2 \cos \theta$ , and that the other  $\theta$ -dependent term can be neglected since it is of  $\mathcal{O}(3)$ , with magnitude proportional to  $\rho_2 b_2^2$ . Hence,  $\theta$  is slowly varying in time, and when integrated against the extremely rapidly decaying factor of  $e^{-18r^2}$  from  $\nabla H$ , only the value of  $\theta(t)$  at  $t=0$  contributes, as may be seen from a steepest descent calculation. Therefore, the  $\theta$ -dependent perturbation terms may be treated as being effectively constant.

*Remark:* In the regime  $\omega = \mathcal{O}(\varepsilon)$ , there are folded singularities on the ring  $C_{SN}$ . Preliminary calculations show that they are directly related to the maximal torus canards. The analysis of these folded singularities and the relationship to torus canards and MMO are the subjects of a separate article.<sup>9</sup>

## VII. MORE GENERAL SYMMETRY BREAKING

In this section, we describe briefly how the results obtained above for system (5) carry over to a rotated planar system of van der Pol type with more general symmetry breaking. As such, we define the new system

$$\dot{r} = r(z - f(r)), \quad (41a)$$

$$\dot{\theta} = \omega, \quad (41b)$$

$$\dot{z} = \varepsilon(a + b\sigma(\theta) - r), \quad (41c)$$

where  $\sigma(\theta)$  is a general, smooth, periodic function of  $\theta \in [0, 2\pi)$ . In this case, the  $z$ -null-surface is  $\mathcal{N}_z = \{(r, \theta, z) | r = a + b\sigma(\theta)\}$ , which is a cylinder of approximate radius  $a$  that is distorted by  $\sigma(\theta)$ . As before, the parameter  $b$  measures the strength of the symmetry breaking. For small  $b$ , system (5) reduces at leading order to Eq. (41) with  $\sigma(\theta) = \cos \theta$ ,

and this linearized system avoids the branch point at  $\{(x, y, z) | x = b, y = 0\}$  present in system (5). We note that, in the slow regime, the analysis of Sec. VI may be carried out for system (41), and one finds that maximal torus canards occur when

$$a = 1 - \frac{\varepsilon}{18} - b\sigma(\theta) + \mathcal{O}(b^2), \quad (42)$$

similar to Eq. (40) but with the function  $\sigma(\theta)$  replacing  $\cos \theta$ , and again with  $b < \varepsilon^{1/2}$ . We also expect that maximal canards persist into the fast  $\omega$  regime, but are less robust to changes in  $a$ , as was the case in system (5).

These expectations are confirmed numerically in Fig. 11, which shows the persistent invariant manifolds  $\mathcal{S}_{a,2}^\varepsilon$  and  $\mathcal{S}_{r,2}^\varepsilon$  on  $\Sigma$  for the case  $\sigma(\theta) = (0.55 + 0.45 \cos \theta) \cos(2\theta - \pi/6)$ . This particular functional form is chosen to break the reflection symmetries of  $\cos \theta$ , and also to introduce additional zeros in  $\sigma(\theta)$ . Figure 11(c) shows the persistent invariant manifolds when  $\omega$  is small. In this regime, Eq. (42) correctly predicts the intersections of the manifolds—both the range in  $a$  over which they persist, and their location in  $\theta_\Sigma$  for any particular choice of  $a$  within this range. The other panels in Fig. 11 show how the persistent invariant manifolds deform as  $\omega$  increases to the fast regime.

## VIII. ROBUST MMO IN THE PURKINJE MODEL

In Sec. IV, we showed that MMO in system (5) can be made more robust by slowing the dynamics of the rotation variable  $\theta$ . In Ref. 36, and as we briefly highlighted in Sec. II, MMO were reported to occur in the Purkinje cell model (2) over a small range in parameter  $J$ , at the transition between the bursting and amplitude modulated states (e.g., Figure 2 of Ref. 36). The analysis presented here for system (5) suggests that to increase the range of  $J$  over which MMO appear in the Purkinje cell model, one should modify the original model in such a way as to decrease the spike frequency. The details of the modification are described in Appendix. The result is a decrease in the typical spiking frequency from about 600 Hz in the original model to about 300 Hz in the modified model—a decrease in the effective  $\omega$  by about 50%.

We plot an example of the voltage dynamics for the modified Purkinje model in Fig. 12. This example illustrates

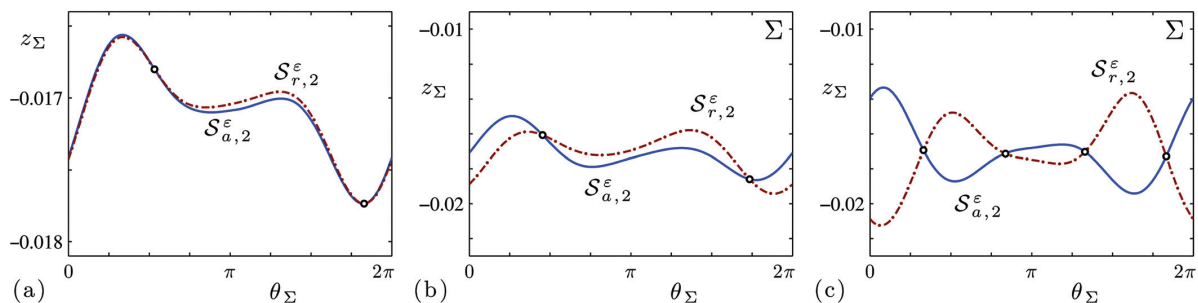


FIG. 11. (Color online) The persistent invariant manifolds of system (41) for the case  $\sigma(\theta) = (0.55 + 0.45 \cos \theta) \cos(2\theta - \pi/6)$ , shown as they cross  $\Sigma$ . The three panels show different regimes for the rotation rate: (a) fast, at  $\omega = 0.9$ ; (b) intermediate, at  $\omega = 0.3$ ; and (c) slow, at  $\omega = 0.01$ . Note the different vertical scale in (a). Other parameters:  $a = 0.99398$ ,  $b = 0.01$ ,  $\varepsilon = 0.1$ .

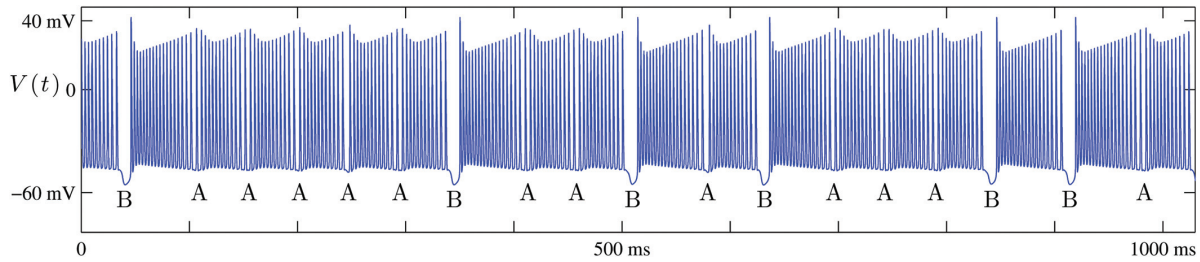


FIG. 12. (Color online) Example of a MMO occurring in the modified Purkinje model of Sec. VIII, with slower fast currents. The choice of  $J = -34.6$  nA results in a complicated pattern of bursts (labeled B) interspersed with amplitude modulation (labeled A).

a complicated MMO, consisting of variable numbers of bursts and amplitude modulations. We find that the range of parameter  $J$  over which these MMO appear is  $\Delta J \sim 0.005$ , an increase of at least two orders of magnitude compared to the range of  $J$  over which MMO occur in the original Purkinje model. These results confirm the prediction of the main model for the biophysical Purkinje model: namely, that slowing the rotation increases the robustness of MMO.

## IX. CONCLUSIONS AND DISCUSSION

In this article, we carried out a study of torus canards, a phenomenon recently reported in a biophysical model of a Purkinje cell.<sup>36</sup> We found it useful to exploit the analogous dynamics for canards in planar systems, such as the van der Pol oscillator, in which a fixed point undergoes a Hopf bifurcation when the null-cline of the slow variable passes a fold in the null-cline of the fast variable. A canard is a trajectory from the attracting slow manifold that spends a long time in the neighborhood of the repelling slow manifold. The family of canards exist in a narrow range of parameter values just beyond the Hopf bifurcation and is associated with rapid growth of small amplitude limit cycles into large amplitude relaxation oscillations. The analogous behavior in one higher dimension is a torus bifurcation of a limit cycle that occurs as the null-surface of a slow variable passes a fold in the null-surface of a fast variable. A torus canard is a trajectory from the persistent invariant manifold of attracting limit cycles that spends a long time in the neighborhood of the persistent invariant manifold of repelling limit cycles. The family of torus canards found nearby the torus bifurcation may exist over a much larger range of parameters and plays an important role in organizing the global behavior of trajectories in the system.

We began with a brief review of the torus canards that exist in the Purkinje cell model. We then showed that torus canards also occur in a much simpler three-dimensional model which consists of a rotated planar system of van der Pol type. In this case, the torus canards are simply copies of the planar canards, trivially extended to a three dimensional phase space by rotation about the  $z$ -axis. The main model considered in this paper is a variation of the rotated planar system, modified to break the rotational symmetry. We did this by introducing a phase-dependent term in the (slow)  $z$ -dynamics. The resulting model, system (5), exhibits nontrivial torus canards.

We studied explicitly how the rotation rate  $\omega$  affects the behavior of torus canards in this model. In the regime of fast

rotation, we showed via the method of averaging that the phase-dependent term shifts the location of the torus bifurcation associated with the torus canards, but that the behavior of the torus canards themselves is otherwise essentially the same as in the planar case. In the regime of slow rotation, we used the method of geometric desingularization (a.k.a., the blow-up method) to identify the particular trajectories on the attracting persistent invariant manifold that correspond to maximal torus canards. These exist over a large range of parameter values and separate orbits which execute a LAO from those which execute a SAO. The coexistence of such orbits results in MMO in the long-time behavior of individual trajectories. The results from the detailed analysis of system (5) carry over to system (41), which includes an arbitrary symmetry breaking term.

Finally, returning to the Purkinje cell model, we determined how to substantially enlarge the parameter interval over which torus canards and MMO occur. This was achieved using insight gained from our elementary model, system (5). These results may be useful for developing a better understanding of transitions between bursting states and amplitude modulated states in this and other models in neuroscience.

## ACKNOWLEDGMENTS

The research of A.M.B., G.N.B., and J.B. was supported by the Center for BioDynamics at Boston University and the NSF (DMS 0602204, EMSW21-RTG). The research of T.K. was supported by NSF-DMS 0606343. M.A.K. holds a Career Award at the Scientific Interface from the Burroughs Wellcome Fund. We thank Mathieu Desroches, Bernd Krauskopf and Hinke Osinga for useful discussions and John Guckenheimer for helpful comments on the manuscript.

## APPENDIX: PURKINJE MODEL

The value of the parameters used in the Purkinje cell model (2) are given in Table I. The equations<sup>51</sup> used for the forward and backward rate functions are

$$\alpha_{\text{CaH}} = k_{\text{CaH}} \frac{1.6}{1 + e^{-0.072(V-5)}}, \quad (\text{A1a})$$

$$\beta_{\text{CaH}} = k_{\text{CaH}} \frac{0.02(V+8.9)}{-1 + e^{(V+8.9)/5}}, \quad (\text{A1b})$$

TABLE I. Parameters used in the Purkinje cell model (2). In addition, we use  $C = 1$  nF for the cell's capacitance.

Channel	Reversal potential (mV)	Conductance ( $\mu\text{m ho}$ )
leak (L)	$V_L = -70$	$g_L = 2$
High-threshold calcium (CaH)	$V_{\text{CaH}} = 125$	$g_{\text{CaH}} = 1$
Fast sodium (NaF)	$V_{\text{NaF}} = 50$	$g_{\text{NaF}} = 125$
Delayed rectifier potassium (KDR)	$V_{\text{KDR}} = -95$	$g_{\text{KDR}} = 10$
M-current (KM)	$V_{\text{KM}} = -95$	$g_{\text{KM}} = 0.75$

$$\alpha_{\text{NaF}} = k_{\text{NaF}} \left[ \frac{1}{1 + e^{(V+59.4)/10.7}} \right] \left[ 0.15 + \frac{1.15}{1 + e^{(V+33.5)/15}} \right]^{-1}, \quad (\text{A1c})$$

$$\beta_{\text{NaF}} = k_{\text{NaF}} \left[ 1 - \frac{1}{1 + e^{(V+59.4)/10.7}} \right] \left[ 0.15 + \frac{1.15}{1 + e^{(V+33.5)/15}} \right]^{-1}, \quad (\text{A1d})$$

$$\alpha_{\text{KDR}} = k_{\text{KDR}} \left[ \frac{1}{1 + e^{-(V+29.5)/10}} \right] \left[ 0.25 + 4.35 e^{-|V+10|/10} \right]^{-1}, \quad (\text{A1e})$$

$$\beta_{\text{KDR}} = k_{\text{KDR}} \left[ 1 - \frac{1}{1 + e^{-(V+29.5)/10}} \right] \left[ 0.25 + 4.35 e^{-|V+10|/10} \right]^{-1}, \quad (\text{A1f})$$

$$\alpha_{\text{KM}} = \frac{0.02}{1 + e^{-(V+20)/5}}, \quad (\text{A1g})$$

$$\beta_{\text{KM}} = 0.01 e^{-(V+43)/18}, \quad (\text{A1h})$$

and the equilibrium function for the fast potassium gating variables is

$$m_{\text{NaF},\infty} = \left[ 1 + e^{-(V+34.5)/10} \right]^{-1}. \quad (\text{A2})$$

The sodium channel is sufficiently fast that we make the standard approximation in Eq. (2a) that  $m_{\text{NaF}}$  takes the value  $m_{\text{NaF},\infty}$ . The constants  $k_{\text{CaH}}$ ,  $k_{\text{NaF}}$ , and  $k_{\text{KDR}}$  are included in Eq. (A1) to adjust the time scales of these currents. In Sec. II, as in Ref. 36, all these constants are set to one. In Sec. VIII, we choose  $k_{\text{CaH}} = 0.9$ ,  $k_{\text{NaF}} = 0.5$ , and  $k_{\text{KDR}} = 0.5$ . Slowing these currents decreases, the characteristic rapid spiking frequency exhibited by solutions from about 600 Hz to about 300 Hz.

<sup>1</sup>V. N. Belykh, I. V. Belykh, M. Colding-Jørgensen, and E. Mosekilde, "Homoclinic bifurcations leading to the emergence of bursting oscillations in cell models," *Eur. Phys. J. E* **3**, 205 (2000).

<sup>2</sup>E. Benoît, "Systemes lents-rapides dans  $\mathbb{R}^3$  et leur canards," *Asterisque* **109-110**, 159 (1983).

<sup>3</sup>E. Benoît, J. F. Callot, F. Diener, and M. Diener, "Chasse au canard," *Collect. Math.* **31-32**, 37 (1981).

<sup>4</sup>K. Bold, C. Edwards, J. Guckenheimer, S. Guharay, K. Hoffman, J. Hubbard, R. Oliva, and W. Weckesser, "The forced van der Pol equation II: Canards in the reduced system," *SIAM J. Appl. Dyn. Syst.* **2**, 570 (2003).

<sup>5</sup>B. Braaksma, "Critical phenomena in dynamical systems of van der Pol type," Ph.D. thesis (Utrecht University, Netherlands, 1993).

<sup>6</sup>M. Brøns and K. Bar-Eli, "Canard explosion and excitation in a model of the Belousov-Zhabotinskii reaction," *J. Phys. Chem.* **95**, 8706 (1991).

<sup>7</sup>M. Brøns, T. J. Kaper, and H. G. Rotstein, "Introduction to focus issue: Mixed mode oscillations: Experiment, computation, and analysis," *Chaos* **18**, 015101 (2008).

<sup>8</sup>M. Brøns, M. Krupa, and M. Wechselberger, "Mixed mode oscillations due to the generalized canard phenomenon," in *Bifurcation Theory and Spatio-Temporal Pattern Formation*, Fields Inst. Communications (Amer. Math. Soc., Providence, RI), Vol. 49, pp. 39-63.

<sup>9</sup>J. Burke, M. Desroches, and T. Kaper, "Folded singularities, mixed-mode oscillations, and torus canards" (unpublished).

<sup>10</sup>P. F. Byrd and M. D. Friedman, "Handbook of elliptic integrals for scientists and engineers," in *Grundlehren der Mathematische Wissenschaften, LXVII* (Springer-Verlag, Berlin, 1954).

<sup>11</sup>G. Cymbaluyk and A. Shilnikov, "Co-existent tonic spiking modes in a leech neuron model," *J. Comput. Neurosci.* **18**, 269 (2005).

<sup>12</sup>M. Desroches, B. Krauskopf, and H. M. Osinga, "The geometry of slow manifolds near a folded node," *SIAM J. Appl. Dyn. Syst.* **7**, 1131 (2008).

<sup>13</sup>M. Diener, "The canard unchained or how fast/slow dynamical systems bifurcate," *Math. Intell.* **6**, 38 (1984)

<sup>14</sup>M. Diener and F. Diener, "Chasse au canard: I-IV," *Collect. Math.* **31-32**(1-3), 37 (1981).

<sup>15</sup>E. J. Doedel, B. E. Oldeman, A. R. Champneys, F. Dercole, T. Fairgrieve, Y. Kurmetsov, R. Paffenroth, B. Sandstede, X. Wang, and C. Zhang, AUTO: Software for continuation and bifurcation problems in ordinary differential equations, available at <http://indy.cs.concordia.ca/auto/>.

<sup>16</sup>F. Dumortier, "Techniques in the theory of local bifurcations: Blow-up, normal forms, nilpotent bifurcations, singular perturbations," in *Bifurcations and Periodic Orbits of Vector Fields*, edited by D. Szolmiuk (Kluwer, Dordrecht, 1993).

<sup>17</sup>F. Dumortier and R. Roussarie, "Canard cycles and center manifolds," *Mem. Am. Math. Soc.* **121**, 577 (1996).

<sup>18</sup>W. Eckhaus, "Relaxation oscillations including a standard chase on French ducks," in *Asymptotic Analysis II, LNM 985* (Springer-Verlag, New York, 1983), pp. 449-494.

<sup>19</sup>G. B. Ermentrout and M. Wechselberger, "Canards, clusters, and synchronization in a weakly coupled interneuron model," *SIAM J. Appl. Dyn. Syst.* **8**, 253 (2009).

<sup>20</sup>N. Fenichel, "Persistence and smoothness of invariant manifolds for flows," *Indiana Univ. Math. J.* **21**, 193 (1971).

<sup>21</sup>N. Fenichel, "Geometric singular perturbation theory for ordinary differential equations," *J. Differ. Equations* **31**, 53 (1979).

<sup>22</sup>F. R. Fernandez, J. D. T. Engbers, and R. W. Turner, "Firing dynamics of cerebellar Purkinje cells," *J. Neurophysiol.* **98**, 278 (2007).

<sup>23</sup>S. Genet and B. Delord, "A biophysical model of nonlinear dynamics underlying plateau potentials and calcium spikes in Purkinje cell dendrites," *J. Neurophysiol.* **88**, 2430 (2002).

<sup>24</sup>S. Genet, L. Sabaraly, E. Guignon, H. Berry, and B. Delord, "Dendritic signals command firing dynamics in a mathematical model of cerebellar Purkinje cells," *Biophys J.* **99**, 427 (2010).

<sup>25</sup>J. Grasman and J. J. Wentzel, "Co-existence of a limit cycle and an equilibrium in Kaldor's business cycle model and its consequences," *J. Econ. Behav. Organ.* **24**, 369 (1994).

<sup>26</sup>J. Guckenheimer, "Singular Hopf bifurcation in systems with two slow variables," *SIAM J. Appl. Dyn. Syst.* **7**, 1355 (2008).

<sup>27</sup>J. Guckenheimer, K. Hoffman, and W. Weckesser, "The forced van der Pol equation I: The slow flow and its bifurcations," *SIAM J. Appl. Dyn. Syst.* **2**, 1 (2003).

<sup>28</sup>J. Guckenheimer and P. Holmes, *Nonlinear Oscillations, Dynamical Systems, and Bifurcations of Vector Fields*, 2nd ed., Applied Mathematical Sciences Series 42 (Springer-Verlag, New York, 1990).

<sup>29</sup>J. Guckenheimer and C. Kuehn, "Homoclinic orbits of the FitzHugh-Nagumo equation: Bifurcations in the full system," *SIAM J. Appl. Dyn. Syst.* **9**, 138 (2010).

<sup>30</sup>E. M. Izhikevich, "Subcritical elliptic bursting of Bautin type," *SIAM J. Appl. Math.* **60**, 503 (2000).

<sup>31</sup>E. M. Izhikevich, "Synchronization of elliptic bursters," *SIAM Rev.* **43**, 315 (2001).

<sup>32</sup>E. M. Izhikevich, *Dynamical Systems in Neuroscience* (MIT, Cambridge, MA, 2007).

<sup>33</sup>E. M. Izhikevich, N. S. Desai, E. C. Walcott, and F. C. Hoppensteadt, "Bursts as a unit of neural information: Selective communication via resonance," *Trends Neurosci.* **26**, 161 (2003).

<sup>34</sup>C. K. R. T. Jones, "Geometric singular perturbation theory," in *Dynamical Systems, Montecatini Terme, LNM 1609* (Springer-Verlag, New York, 1995), pp. 44-120.

<sup>35</sup>C. K. T. Jones and S.-K. Tin, "Generalized exchange lemmas and orbits heteroclinic to invariant manifolds," *Discrete Contin. Dyn. Syst., Ser. S* **2**(4), 967 (2009).